Metabolic adaptation pilots the differentiation of human hematopoietic cells

Laëtitia Racine[1,2,3,4], Romuald Parmentier[1,2,3,4], Shreyas Niphadkar[5], Julie Chhun[1,2,3,4], Jean-Alain Martignoles[1,3,4], François Delhommeau[1,3,4], Sunil Laxman[5], Andras Paldi[1,2,3,4*]

[1]*Sorbonne Université, INSERM, Centre de Recherche Saint-Antoine, CRSA, 75012, Paris*
[2]*Ecole Pratique des Hautes Etudes, PSL Research University, Paris, France*
[3]*AP-HP, SIRIC CURAMUS, Hôpital Saint-Antoine, Service d'Hématologie Biologique, 75012, Paris*
[4]*OPALE Carnot Institute, Paris, France*
[5]*Institute for Stem Cell Science and Regenerative Medicine (DBT-inStem), GKVK Post Bellary Road Bangalore, 560065 India*
** corresponding author: andras.paldi@ephe.psl.eu*

Abstract

A continuous supply of energy and metabolic intermediates is an essential prerequisite for survival and the highest priority for the cell. We hypothesize that cell differentiation is a process of optimization of energy flow in a changing environment through phenotypic adaptation. A mechanistic basis of this hypothesis is provided by the established link between core energy metabolism and epigenetic covalent modifications of chromatin. This hypothesis predicts that early metabolic perturbations impact subsequent differentiation. To test this, we induced transient metabolic perturbations in undifferentiated human hematopoietic cells using pharmacological inhibitors targeting key metabolic reactions. We recorded changes in chromatin structure and gene expression, as well as phenotypic alterations by single-cell ATAC and RNA sequencing, time-lapse microscopy and flow cytometry. Our observations suggest that these metabolic perturbations are shortly followed by alterations in chromatin structure, leading to changes in gene expression. We also show that these transient fluctuations alter the differentiation potential of the cells.

Introduction

The structural and functional reorganization during cell differentiation is a metabolically demanding process. Many proteins and other macromolecules are replaced, and the cytoskeleton is reorganized leading to changes in the cell's shape and motion. As the gene expression profile is modified many new genes that are transcribed, while other genes become repressed. This change in gene expression is invariably preceded by substantial chromatin remodeling initiated by epigenetic modifications [1]. Cell differentiation is also accompanied by a metabolic transition from a predominantly glycolytic regime to an oxidative one [2]. As is true for any change in a cell, these modifications would be impossible without mobilizing important internal metabolic resources. Biosynthetic reactions of mRNA, protein and other macromolecular synthesis are run by the hydrolysis of the high energy bond of ATP and other trinucleotide phosphates, others are driven by the transfer of electrons from reduced transporters such as NADH, NADPH or $FADH_2$. The energy demand is assumed to be particularly high in the case of chromatin remodeling required for changes in gene expression, because epigenetic modification reactions that determine chromatin stability represent a substantial energetic cost [3]. These covalent modifications require different high energy substrates, particularly SAM and acetyl-CoA, which serve as donors to provide methyl and acetyl groups for histone and DNA methylation and acetylation. NAD^+, FAD and α-ketoglutarate, among others, are substrates required for reversal reactions that remove these groups from DNA and histones. Due to the rapid turn-over of these modifications [3–5], the demand for the high energy substrates is permanent even if the overall epigenetic profile remains globally unchanged and may substantially increase during major structural changes that accompany cell differentiation. This dependency of epigenetic modifications on the key metabolites therefore links the chromatin state to the metabolic state of the cell. The intracellular metabolite abundances are determined by the carbon and energy flux through their respective pathways. The flux through a given pathway is in turn determined by the availability of the initial substrates and electron donors, the terminal electron acceptors, and the thermodynamic gradient defined by them [6]. Most carbon sources and terminal electron acceptors are derived from the environment. Maintaining a constant energy flux requires continuous adjustment of the metabolic network to the fluctuations of the substrate concentrations in the given environment. Paradoxically, the metabolic activity of the cells itself may contribute to local changes in substrate concentration. Small fluctuations can be rapidly buffered by the highly interconnected network [7].

Nevertheless, buffering alone is insufficient to compensate the stress induced by large fluctuations, that can come externally due to environmental changes and internally with metabolic state shifts. Metabolic flux changes can happen through mass action and allosteric changes, along with changes in gene expression that enable cells to stably reorganize these fluxes. Collectively this will enable cells to metabolize new substrates or to migrate to a new environment. Given the highly interconnected nature of the metabolic network, fluctuations in one of the pathways inevitably impact all the others. The more extensive the reorganization of fluxes, the greater the impact on the intracellular concentration of "sentinel metabolites" strategically positioned at the crossroads of the major catabolic and anabolic pathways [8].

Due to the link between the "sentinel metabolites" and epigenetic modifications, metabolic fluctuations can be conveyed to the chromatin by modifying the dynamic balance of epigenetic reactions. A key question is defining what can be considered as a "large" metabolic fluctuation. While it is difficult to set a clear limit in term of intracellular metabolite abundances, large perturbations can be detected based on their immediate phenotypic effects on cell division rate and growth. These processes require additional energy and carbon resources and serve as a reliable proxy for tracking the overall metabolic state. Chromatin remodeling, a prerequisite for changing the gene expression patterns and, consequently, cell differentiation, consumes a substantial portion of the cell's energy production [3,8]. Therefore, it is reasonable to hypothesize that metabolic stress and cell differentiation are not only coupled, but the former triggers the latter. To assess our hypothesis, we used human cord blood derived $CD34^+$ cells. Recent studies have shown that major changes occur during the first 24 to 96 hours following the *in vitro* stimulation of these cells [1,9]. The earliest changes involve rapid and extensive non-specific chromatin opening, rendering most gene promoters in the genome accessible for transcription. Consequently, by the end of the first cell cycle, approximately 48h later, cells enter a phase of quasi-random hyper-transcription. This state is referred to as the "multilineage primed state" due to the simultaneous expression of genes characteristic to concurrent cell lineages. It serves to prepare the cells to respond to a variety of environmental changes. In the hematopoietic cells used in our studies, this process spans several cell cycles and is characterized by strong morphological fluctuations [9]. By the end of the first two-three cell cycles, between 72 and 96h post stimulation, distinct gene expression profiles start to emerge, indicating that the cells are about to complete the first stage of the fate decision process. It is also known that multipotent hematopoietic cells and lineage committed progenitors display markedly distinct metabolic characteristics [10–15]. Does the change of the metabolic setup of the cells precede and trigger the non-specific chromatin opening? If so, does the nature of metabolic stress impact the cell fate decision process?

To test our hypothesis regarding the role that metabolic stress plays in initiating and driving cell differentiation, we partially and transiently inhibited different essential metabolic pathways using small molecular inhibitors. Subsequently, we evaluated the short- and long-term consequences on the proliferation and differentiation of the cells *in vitro*.

The cell's energy metabolism relies on three major energy and carbon sources: glucose, amino acids (primarily glutamine) and lipids [16]. In the present study, we specifically investigated the roles of glucose and glutamine. The targeted metabolic pathways along with the inhibitors used are schematically represented in **S1 Fig**. We used 2-deoxy-D-glucose (2-DG) to inhibit the first step of glucose utilization by glycolysis, thereby reducing all downstream processes. This reduction of glycolysis diminishes ATP production and is expected to shift the balance of $NADP^+$/NADPH toward a more reduced state. Indeed, the pentose-phosphate pathway is the major source of NAPDH, an essential electron donor in lipid biosynthesis. The contribution of glucose to the carbon flow through pyruvate and acetyl-CoA to lipid biosynthesis and the Krebs cycle is also expected to decrease.

The second inhibitor, 6-Diazo-5-oxo-L-norleucine (DON), inhibits the conversion of glutamine to glutamate by the glutaminase (GLS). Glutamine plays a very important role in cellular

metabolism by providing carbon and nitrogen to directly fuel biosynthetic processes in the cytoplasm, such as the biosynthesis of nucleotides or glutathione. After import into the mitochondria through a glutamine transporter and deamination to glutamate by GLS, glutamine-derived carbon atoms enter the TCA cycle and are used either for ATP production by terminal oxidation or for biosynthetic processes. DON might perturb all these downstream processes. However, glutamine is a non-essential amino acid that can be synthetised by the cell. Therefore, the effects of DON re more complicated and will at least partially be mitigated by the alternative amino acid sources.

To perturb the entire glutamine pathway in a more targeted way, we used aminooxyacetate (AOA) to inhibit the glutamate-pyruvate and glutamate-oxaloacetate aminotransferases [17]. These enzymes are essential because they ensure the redistribution of nitrogen between the amino acids and produce α-ketoglutarate (often referred as αKG), a sentinel metabolite and essential TCA cycle intermediate. In this way, glutamine supplies carbon for ATP production by terminal oxidation or for biosynthesis of sugars and lipids. It also serves as a substrate for histone and DNA demethylation, thereby directly impacting chromatin structure.

All three drugs are known to induce substantial perturbation of the cellular energy metabolism and interfere with differentiation of hematopoietic cells [18]. Here, we investigate the immediate effects of metabolic perturbations induced by these inhibitors on the $CD34^+$ cells at the moment of cytokine stimulation, their consequences on the initial steps of cell fate decision and the long-term impact on differentiation.

We used time-lapse microscopy, cytometry with a generation tracker, single-cell and bulk ATAC-seq, and single-cell mRNA sequencing. The short-term effects of these perturbations on the cell proliferation and morphology, the dynamics of the chromatin structure and the gene expression were recorded. The potential long-term effects on differentiation capacity resulting from transitory inhibition were studied after *in vitro* culture.

Results

The experimental strategy shown on **Fig.1A** was based on the hypothesis that early metabolic priming impacts the fate choice of the cells at later stages. First, we followed the cell's dynamic behavior and morphologic changes under various metabolic conditions during the earliest stages following the cytokine stimulation at 0h (see **Material and Methods**). We utilized targeted, quantitative mass spectrometry to assess the general changes in cell metabolism after inhibitor treatment. Subsequently, the early chromatin changes were identified using bulk and single-cell ATAC-seq at different time points during the first 24 hours. To assess whether the cellular phenotype is under the influence of prior metabolic changes, the gene expression patterns were sampled at 96h post stimulation using single-cell RNA sequencing. Finally, the differentiation potential of the cells was assessed at later time points by flow cytometry using a set of cell surface markers. To do this, the cells were first cultured in the presence of inhibitors for a period of 4 days then, transferred to a new medium without inhibitors and a different cytokines composition (see **Material and Methods**) for an additional 10 days. Cell surface marker characterization was performed for each condition at day 4, 7, 10 and 14.

Early metabolic perturbation strongly affects cell behavior

In a pilot study we determined the sub-lethal concentrations that allowed survival of about half of the treated cells (1mM 2-DG, 2.5µM DON and 1.9mM AOA). We assume that at this concentration, the targeted pathways are only partially inhibited in the surviving cells. At 24h, small molecular metabolites were extracted from ~10^5 cells after rapid quenching (see **Materials and Methods**) and analyzed by targeted, quantitative mass spectrometry [19]. The cumulative normalized results of 9 experiments shown on **S2 Fig.** indicate that the use of inhibitors induced substantial metabolic perturbations. We measured the relative amounts per condition of 11 metabolites: pyruvate, lactate, citrate, α-ketoglutarate, malate, succinate as indicators of the glycolytic and the tricarboxylic acid cycle activity, as well as amounts of aspartate, tyrosine, glutamine, and the pair S-adenosylhomocysteine (SAH)/S-adenosyl-methionine (SAM). The relative amounts of all these metabolites were significantly altered compared to the control condition, and the responses were distinct depending on the enzyme inhibitor used. To make sense of and interpret these changes we must consider the interconnected nature of the metabolic network, and its complex behavior. While targeting specific enzymes (**S1 Fig**), the inhibitors are also expected to have wide-ranging pleiotropic effects, making it challenging to predict how individual metabolite abundances will change. Nevertheless, our measurements reveal significant alterations compared to the control, indicating real, substantial metabolic perturbations that are induced by the stress. Different inhibitors induced various alterations, and we also observed high sample-specific variations. Given the heterogeneous constitution of the $CD34^+$ cell population, we postulate that the cells developed multiple adaptation strategies exhibiting a broad spectrum of responses for the diverse metabolic impairments induced by the inhibitors.

We characterized the cells by using flow cytometry with Cell Trace Violet labeling to track the number of cell divisions, and the evolution of the multipotent cell markers CD34 and CD133 during the first 96hrs following stimulation. A representative example is displayed on **Fig.1B**. Similar tendency was observed in all donors with some differences in kinetics (**S3 Fig.**). As described previously, the untreated control cells underwent one or two divisions, with only a small proportion of them dividing three or four times [9]. The cells treated with 2-DG followed roughly the same scheme but divided much slower. Indeed, the proliferation index of 2-DG treated cells was only 1.28 when untreated cell's one was 3.46 (**S1 Table**). DON and AOA strongly inhibit cell divisions. Only half of the cells treated with DON made a single division, the second half remained undivided for 96h whereas cells treated with AOA did not divide at all (**Fig.1B**). As expected, the CD34 marker decreased at each cell division in all conditions. Overall, both the inhibition of glycolysis and glutaminolysis accelerated this process (**S1 Table**). CD133 followed similar dynamics, however its complete loss was more rapid with about half of the cells becoming negative after few divisions. CD133 decreased only slightly in DON treated cells whereas AOA treated cells almost completely lost this marker even without division. The most significant impact is observed in the presence of 2-DG where the loss of the marker was reached after the first division.

To further characterize the dynamic behavior of the cells during the same 96h period but also beyond this time-window, we made time-lapse records of individual cells during a period of 6 days with a frequency of an image every 2 minutes (see **Material and Methods**). The cumulative counts of the number of living cells, cell deaths and cell divisions are shown on **Fig.1C**. Representative videos are shown in **S1 Movie**. All conditions invariably exhibited a short initial period of high cell death rate typical to this type of experiments, generally attributed to the backlash of cell thawing. However, the cell survival at later stages was substantially different between each of the inhibitor treated conditions. After a long 48-hour first cell cycle, non-treated cells divided regularly with low death rate, and the population increased exponentially. Cells treated with 2-DG also started to divide after 48h, but the rate of cell divisions remained low, and the death rate remained high. As a result, the population size remained largely unchanged during the entire recording period. In contrast, the cellular dynamics was very different in the case of DON and AOA. The first divisions of both the DON- and AOA-treated cells were observed relatively late, occurring approximately between 70h to 90h. The initial death rate of DON-treated cells was much higher than in the other conditions. However, it decreased after the first division, coinciding with an increase in the division rate. From this point onward, DON-treated cells exhibited a higher proliferative rate compared to the control group suggesting potential cellular adaptation to the metabolic stress. The death and division rate of the AOA-treated cells remained consistently high resulting in a population with a cumulatively low cell density.

Previous observations have shown that $CD34^+$ cells adopt two morphological phenotypes, either round or polarized. A large fraction of the cells was able to switch with high frequency between the two forms. The stabilization in either of these phenotypes is associated with the emergence of distinct transcriptional profiles [9]. Thus, we examined if the metabolic stress influenced the fluctuating behavior of the cells. To do this, we tracked the cells on the time-lapse records and counted the number of morphologic switches. Despite a significant heterogeneity between the clones, we observed an overall trend at the population level. As

shown on **Fig.1D**, the switch frequency of AOA and DON treated cells increased slightly but significantly compared to the controls, while the frequency of the 2-DG cells was slightly lower.

Taken together, the initial observations show that the inhibitors induce rapid, substantial metabolic perturbations within the first few hours following cell stimulation. These perturbations alter essential metabolite levels in the cells, impact the cell viability and division and induce phenotypic changes. We are aware that critical chromatin changes are known to occur during the first 24hrs [1]. Therefore, we sought to assess how the chromatin structure responds to the metabolic perturbations and how these perturbations impact the gene expression.

Initial metabolic stress impacts chromatin accessibility and gene expression.

We investigated the genome-scale changes of the chromatin structure using whole cell population-level ATAC-seq (referred to as bulk ATAC-seq) at 0h, 3h, 12h and 24h after the stimulation of the cells. First, we recorded the number of accessible DNA regions (peaks) in each condition and at each time point (**Fig.2A**). As expected, based on our previous study, we observed a sharp increase of the number of peaks simultaneously with the stimulation of the cells. This increase, comparable to the control in all conditions, is the consequence of the global non-specific chromatin decompaction characterized earlier [1]. Between 3h and 24h the number of peaks remained stable or decreased slightly. The largest decrease, about 13%, was observed in AOA-treated cells meaning that the chromatin remained slightly more compacted than in controls. A possible explanation could be the change of metabolic substrate availability required for chromatin opening.

Next, we analyzed how the size of common peaks between control and each condition changed over time. As a proxy for the size of a peak, we used the number of sequenced reads (read counts) that define it. The increase or decrease in read counts for a peak in the same genomic position was interpreted as the likelihood of the chromatin to open or close. We calculated the log-fold changes of the number of reads of each peak between conditions and the associated p-values. The pairwise comparisons at all time points are represented as volcano plots in **S4 Fig**. Overall, the number of peaks with increased or decreased size was found equilibrated with the significant exception of AOA-treated cells at 24h. Here, the number of peaks with decreased size compared to the control was strikingly high.

To establish if the metabolic perturbations also induced modifications in the pattern of accessibility, we performed principal component analysis (PCA). The PCA plot on **Fig.2B** shows that both the control and inhibitor treated cells undergo rapid and similar changes between 0h and 3h. At 12h control cells are clearly separated from the other three conditions. 24h after stimulation AOA-treated cells are clearly separated from the two other conditions and map to the opposite position of the control untreated cells (**Fig.2B**). The analysis confirms that global rearrangement of chromatin after cell stimulation happens at the same rapid rate and to the same extent in all conditions, but the pattern of it starts to diverge soon after. In addition, it shows that the effect of the metabolic perturbations is clearly detected at 12h and

results in a substantially different pattern after 24 hours. AOA-treated cells have not only the lowest number of accessible DNA regions, but also have a different pattern compared to the other two conditions or the control.

To further characterize these differences, we performed single-cell ATAC-seq on the cells at 24h, when the changes were the most noticeable in the bulk analysis. In accordance with our previous study [1], the single-cell ATAC approach successfully identified the peaks also detected by the bulk version. The cumulative peak numbers confirmed the lower total number of peaks in AOA-treated cells compared to the other conditions. This results from the lower number of accessible DNA regions in individual cells (median count to 14155 peaks per cell for AOA condition versus 16973 to 18913 peaks per cell for other conditions, see **S2 Table**).

To assess the heterogeneity of the chromatin response to metabolic perturbations, we visualized the cells on the same UMAP projection (**Fig.2C**). The four conditions showed different and heterogenous profiles. Overall, 16 clusters were found and numbered from 0 to 15 (**Fig.2D**). The first 6 large clusters totalized around 90% of the cells, while the remaining eleven contained only a few percent each. All but one cluster contained cells from each condition, but the distribution of the control and treated cells was unequal between the different clusters (**Fig.2E**). This reveals that the different perturbations generated partially different patterns. This was particularly true for the AOA-treated cells. The largest cluster (n°0) contained no AOA-treated cells while the control, 2-DG and DON-treated cells were represented at roughly equal proportion. The composition of the cluster n°1 was very similar with only 6.5% of AOA-treated cells contrary to the +/- 30% of cells of the other conditions. By contrast, AOA-treated cells dominated the clusters 3, 4 and 8. Cluster n°2 and 5 were composed of roughly similar proportions of control and metabolically perturbed cells of the three types.

The single-cell ATAC-seq results confirmed that as suggested by the bulk ATAC-seq analysis, the different metabolic perturbations generated different chromatin responses. The response to each condition was heterogenous. Six major cell clusters with different chromatin profiles suggested that the same type of perturbation induced a heterogenous but overlapping range of chromatin responses. The proportion of the cells giving one or the other of the six responses varied between the conditions. To investigate the potential biological consequences of these differences, we extracted the list of differentially accessible peaks for each cluster. We assigned the closest genes to each peak and performed a Gene Ontology analysis on the gene lists. We focused on the first six clusters, because they contained most of the cells for all conditions. Results (**S5 Fig.**) showed that all clusters displayed high accessibility of genomic regions associated to biological process typical for cells in growth and division, such as “positive regulation of cellular biogenesis”, “regulation of cellular component size”, “cell adhesion” or “cell communication”. In clusters n°3 and 5, lymphoid or myeloid associated processes were also detected (“T cell differentiation” p_{adj} = 2.64e-23, “lymphocyte differentiation” p_{adj} = 2.64e-23, “mononuclear cell differentiation” p_{adj} = 4,80e-22, “myeloid leukocyte activation p_{adj} = 5.91e-14). It appears therefore, that the cells’ response to the

metabolic perturbations is partially overlapping and heterogeneous with a varying fraction of cells providing a similar response in each condition. Here again, the response to AOA appears substantially different than the other inhibitors. It is worth reminding that, at this stage, despite the differences between conditions, the number of accessible promoters in the cells exceeded largely the maximal number of genes expressed in individual cells. The promoter accessibility is not the limiting factor responsible for restriction of gene transcription. However, the different chromatin profiles induced by the metabolic perturbations may channelize the subsequent evolution of the chromatin to later stages when the accessibility becomes a restrictive factor for gene transcription.

To verify if this is indeed the case, we analyzed the transcriptomes by single-cell mRNA sequencing of the cells combined with epitopes detection (CITE-seq) at 96h post-stimulation. At this time point, the cells in each condition had recovered from the initial perturbation, entered a phase of growth and proliferation (**Fig.1C**) and some of them went through the first steps of fate commitment [9]. We analyzed 5000 cells from each condition using the Chromium 10X technology. After quality control filters, normalization and alignment of the sequences on the genome, the data from the control and the perturbed conditions were integrated and we visualized the structure of the cell populations using the usual dimension reduction approach (UMAP) (**Fig.3A**). The gene expression profiles generated in response to AOA, 2-DG and DON were heterogenous but partially overlapped with the control and each other. Overall, 17 clusters with varying number of cells were identified (**Fig.3B**). The distribution of the control and treated cells in the clusters was uneven (**Fig.3C**). 4 clusters were entirely composed of AOA treated cells (clusters n°8, 11, 14 and 15). 10 of the 17 clusters contained no AOA-treated cells and 2 had only a small contribution of them. 2-DG treated cells were overrepresented in clusters 2 and 10 but almost absent from clusters 0, 6 and 9. DON treated cells were overrepresented in clusters 1 and 5, underrepresented in cluster 2 and almost similar to control cell distribution in other clusters. Each cluster had its own set of differentially expressed genes (**S6 Fig.**). Therefore, the cell's chromatin response to the metabolic perturbations at early stages was passed on to the gene expression profile at 96h and generated a heterogenous transcriptomic response dependent of the type of the metabolic stress. The mRNA profile of the AOA treated cells showed the highest difference compared to the other conditions.

To assess the abundance of the CD34 and CD133 proteins on the cell's surface simultaneously with the RNA sequencing we used CITE-seq (**S7 Fig.**). Remarkably, the expression of these markers was the highest in the clusters 0, 6 and 9 where AOA and 2-DG treated cells were absent or underrepresented. These clusters, essentially composed of control and DON-treated cells, may represent the cells with phenotypes close to the pluripotent progenitor cells.

To better characterize the differences between the conditions, we performed pathway and GO analysis of the transcriptomes. We assessed pathway-level differences between the control and metabolically perturbed cells using ReactomeGSA [20]. This approach performs the differential expression analysis directly on the pathway level. It detects small synchronous

changes within a pathway that may reveal a biologically important effect. The results shown on the **Fig.3D**. indicated that AOA treated cells displayed very different pathway activities compared to all the other conditions. Pathways related to “integration of energy metabolism”, “cellular response to starvation”, “glycogen breakdown” and “amino-acid transport across the plasma membrane” were significantly upregulated in the AOA treated cells. Pathways related to epigenetics such as “DNA methylation”, “acetylation” or “pyruvate metabolism and citric acid cycle”, “heme biosynthesis”, “pentose phosphate pathway” among others, were downregulated. These changes are indicative of a deep metabolic reorganization and difficulty to mobilize energy resources. Interestingly, DON-treated cells presented a very different profile with among others, upregulated “epigenetic regulation of gene expression”, “DNA methylation” and “acetylation” pathways and downregulated “glutamate and glutamine metabolism”. Without surprise, 2-DG-treated cells showed a different profile with increase in “glutathione biosynthesis”, “metabolism of porphyrin” or “heme biosynthesis”. Overall, the largest difference was observed between the AOA condition and the control. The GO analysis of differentially expressed markers between conditions (**S3 Table**) showed that compared to control cells, 2-DG-treated cells displayed enriched gene expression in categories related to erythrocyte activity (“oxygen transport” p_{adj} = 0.002, “hemoglobin complex” p_{adj} = 3e-04, “oxygen carrier activity” p_{adj} = 5e-04, “oxygen binding” p_{adj} = 0.003, “heme binding” p_{adj} = 0.03) whereas those related to monocytes or T lymphocytes were underrepresented (“regulation of monocyte differentiation” p_{adj} = 0.008, “monocyte differentiation” p_{adj} = 0.02, “T cell differentiation” p_{adj} = 0.02). In DON-treated cells’ transcriptome, LT cells associated terms seems numerous in the underrepresented categories (“regulation of activated T cell proliferation” p_{adj} = 0.03, “activated T cell proliferation” p_{adj} = 0.03, “T cell mediated immunity” p_{adj} = 0.04, “lymphoid progenitor cell differentiation” p_{adj} = 0.04). However, a wide variety of terms associated with other lineages can be found in the overrepresented list, such as markers related to oxygen transport (“oxygen carrier activity” p_{adj} = 0.008, “oxygen binding” p_{adj} = 0.01, “oxygen transport” p_{adj} = 0.004), megakaryocyte and platelet differentiation (“megakaryocyte differentiation” p_{adj} = 0.01, “platelet aggregation” p_{adj} = 0.01), leukocyte activities (“positive regulation of leukocyte cell-cell adhesion” p_{adj} = 0.04), and overall early differentiation (“hematopoietic stem cell differentiation” p_{adj} = 0.02). Markers for oxygen transport and megakaryocyte differentiation were underexpressed in AOA-treated cells (“oxygen transport” p_{adj} = 0.009, “hemoglobin complex” p_{adj} = 1e-04, “regulation of megakaryocyte differentiation” p_{adj} = 0.02) while those related to leukocyte cells were largely enriched with around twenty associated terms extracted (“myeloid leukocyte migration” p_{adj} = 0.02, “regulation of leukocyte cell-cell adhesion” p_{adj}=0.04, “leukocyte mediated immunity” p_{adj} = 6.4e-08). The enriched categories remain quite diverse, with references to immune system (“antigen processing and presentation” p_{adj} = 1e-06) but also references to LT cells both in enriched and non-enriched categories, suggesting heterogeneity within the population. These observations showed that the cells adopted very different and complex gene expression strategies to overcome the constraints and start to proliferate.

Collectively, the ATAC-seq and RNA-seq studies revealed that early chromatin response to metabolic perturbation is followed by a reinforced transcription response at a

later stage. Even though the chromatin opening is widespread in all conditions at 24h, we observed a certain heterogeneity between and within the conditions. More particularly, the ATAC profile in AOA-treated cells was markedly different compared to the other conditions. This tendency was reinforced when the transcriptome of the four conditions were compared at 96hrs. To evaluate the potential long-term consequences of this metabolic priming, cytometry experiments were carried out at later time points.

Transitory metabolic perturbation has long-term effects on cell differentiation.

After the initial period of 96h in the presence of inhibitors, cells were transferred to a fresh inhibitor-free culture medium for an additional 10 days. To assess the lineage commitment of the cells, the expression of several hematopoietic lineage markers (CD133, CD14, CD15, CD19, CD36, CD41, CD45) was measured by flow cytometry on days 4, 7, 10 and 14. The analysis on day 4 confirmed the CD133 expression pattern detected by cytometry (**Fig.1B**) and the high mortality rate in AOA- and 2-DG-treated cells already observed by time lapse (**Fig.1C**). We found that the higher-than-normal mortality rates also persisted after day 4, even if the inhibitor was no longer present in the culture medium (**Fig.4A**). Importantly, we also discovered that the specific nature of transient metabolic perturbations preceding the initial fate determination influenced the differentiation pathways that the cells followed after the inhibitors were removed.

The dynamical evolution of individual markers and their combinations are shown on **Fig.4** and **Fig.5**. In addition to the high mortality all along the experiment (**Fig.4A**), AOA-treated cells showed the biggest differences compared to the controls. The CD133 level was already lower than in the controls and other treated cells on day 4 and remained low on day 7. AOA-treated cells exhibited a relatively low expression levels of CD45 and CD36, and a fluctuating dynamic of CD15. The proportion of cells with the combination of $CD45^+$ and $CD36^-$ associated with leucocyte (granulocytes and lymphocytes) differentiation was lower than in the control on days 4 and 7, but increased later. Within this group, the $CD45^+CD36^-CD15^+$ cells typical for the granulocyte path were overrepresented during the first two time points and approached the control proportion in the later stages. The fraction of cells with typical monocytic markers was also variable. The $CD45^+CD36^+$ cells consistently showed lower representation at all time points compared to the control condition. However, the proportion of $CD14^+$ monocytes within this population was significantly elevated on day 4 and 7 but dropped below the control level on day 10 and 14. Such a variable expression may reflect a change in the marker expression in the cells but also a variable proliferation capacity of the subpopulation. No erythrocyte progenitors were detected in AOA-treated cells, however a substantial proportion of $CD45^-CD36^-$ cells appear to persist over time. Overall, the differentiation of the AOA-treated cells appears to be truly disturbed even after the removal of the metabolic inhibitor.

Transient 2-DG treatment also strongly influenced the differentiation potential of the cells. These cells also had a higher death rate than the control cells. The CD36 marker showed a sharp transient increase on day 7 with more than 50% of the cell population expressing it. It is worth mentioning that CD36 is required for free fatty acid uptake, and the transition from

glycolysis towards β-oxidation of fatty acids by undifferentiated hematopoietic cells [21]. Expression of CD36 may represent a metabolic adaptation strategy that helps avoiding energy shortage due to the inhibition of glycolysis by increasing fatty acid oxidation [22]. $CD41^+$, $CD45^-CD36^+$ and $CD45^-CD36^-$ cells are slightly more represented compared to controls. The most significant effect of the metabolic perturbation was observed on marker combinations representative of the myeloid and the lymphoid branches. There is a significant decrease in the number of $CD45^+CD36^-$ cells starting from day 7 compared to the control group, although this decrease becomes less pronounced over time. However, the $CD45^+CD36^-CD15^+$ granulocytes remain underrepresented within this population until day 14. Additionally, there is a notable increase in the number of $CD45^+CD36^+$ cells on day 7. However, unlike what was observed with AOA treatment, the $CD14^+$ cells within this population are underrepresented.

As we have shown earlier, DON-treated cells recovered normal morphological phenotype and proliferation capacity from the initial metabolic stress caused by the inhibition of the glutaminase around 96hrs (**Fig.1BC**). Although we observed minor effects on the chromatin structure at 24hrs (**Fig.2**) and on the gene expression profile at 96hrs (**Fig.3**), these cells showed overall similar pattern of commitment as the control cells as witnessed by the cell surface markers distributions (**Fig.4 and 5**). A potential explanation for this full recovery could be the fact that glutamine is a non-essential amino acid.

These observations are in line with the pathway and GO analysis of the transcriptomes shown earlier. They indicate that a transitory perturbation of important metabolic pathways of glucose and glutamine utilization can modify the cell's capacity to divide and differentiate long after the initial trigger is removed.

α-ketoglutarate can compensate some but not every metabolic perturbation.

Overall, general cellular responses to the three tested metabolic perturbations were highly distinct. Throughout the initial 96-hour period of cell culture, it became apparent that cells encountered greater challenges in overcoming the perturbations caused by the inhibition of glutaminase with DON or transaminases with AOA compared to the perturbation affecting glucose metabolism induced by 2-DG (**Fig.1BC**). However, beyond this phase, DON-treated cells appeared to recover and acclimate to their new environment. We observed no substantial variations in terms of fate commitment compared to control cells over the next ten days of *in vitro* culture. In contrast, 2-DG- and AOA-treated cells remained durably affected.

Glucose and glutamine are metabolised through two separate pathways. 2-DG inhibits the first pathway, while DON and AOA impede the latter one. Both pathways feed in the TCA cycle and generate α-ketoglutarate. This metabolite can either be oxidized and contribute to the ATP production or metabolized reductively to generate acetyl-CoA. In addition, it plays a crucial role as a bridge connecting energy metabolism and chromatin-modifying epigenetic mechanisms, serving as a substrate to DNA- and histone-demethylating enzymes. To highlight the role of this metabolite we conducted rescue experiments with αKG to ascertain whether

the inhibitors' effects could be mitigated or compensated for. To do this, we supplemented the culture medium with αKG and repeated the experiments conducted at 96hrs and beyond.

When analysed by cytometry at 96h, the CD133 and CD34 distribution and proliferation capacity of the αKG-supplemented AOA-treated cells were essentially undistinguishable from the normal control cells (**Fig.6A and S1 Table**). Study of transcription profiles by scRNA-seq showed a remarkable restoration in gene expression profiles in AOA-treated cells, marked by the disappearance of the specific AOA profiles and a return of most of the profiles seen in the control condition. However, the transcription profile of the cells remained partially different. αKG supplemented AOA-treated cells are nearly absent from the cluster n°2 and overrepresented in cluster 4 (**Fig.6B**). The metabolic pathway analysis of the scRNA-seq data also indicated a strong αKG effect. The activity of the gene pathways related to various metabolic processes down-regulated in the AOA-treated cells raised to a higher level than in the control cells with αKG (**S8 Fig**). The GO analysis of the differentially expressed genes also confirmed that the effect of αKG is more complex than simple compensation of the transaminase inhibition. Markers for oxygen transport that were under-expressed in AOA-treated cells became now positive markers of AOA+αKG cells ("oxygen transport", p_{adj} = 0.001, "hemoglobin complex" p_{adj} = 4e-04, "oxygen binding" p_{adj} = 0.005). Conversely, several enriched gene categories in AOA-treated cells related to lymphocyte and leukocyte differentiation became now part of the negative markers ("T cell activation" p_{adj} = 4e-06, "regulation of leukocyte cell-cell adhesion" p_{adj} = 5e-07). Some categories remained positive in both conditions ("positive regulation of lymphocyte activation" p_{adj} = 0.03, "dendritic cell migration" p_{adj} = 0.007, "myeloid cell homeostasis" p_{adj} = 0.03). Contrary to the transcription profile, αKG completely erased the effects of AOA treatment on the long-term differentiation capacity of the cells. We observed similar cell surface marker levels and combinations as on the control untreated cells (**Fig.6C and S9 Fig**). The fact that αKG could rescue the proliferation and differentiation capacity of AOA-inhibited cells without fully restoring the gene expression profile identical to the untreated cells shows that alternative gene expression profiles and pathways can lead to a similar biological outcome and suggests a complex relationship between the metabolism, gene expression and differentiation.

αKG improved the proliferation capacity of the 2-DG-treated cells and restored the expression pattern of CD133 (**Fig.6A**). As shown by the UMAP representation, the gene expression pattern of the 2-DG+αKG cells was also like the control cells. The introduction of αKG allowed the restoration of cell populations that were otherwise diminished when exposed solely to the inhibitor (clusters 0, 6, and 9), and reinstated a more balanced distribution of cells within clusters. The pathway and GO analysis showed that the activity of several pathways was reversed by αKG (**S8 Fig. and S4 Table**). Several gene ontology categories linked to erythrocyte activities, which exhibited high activity in 2-DG-treated cells, were downregulated in 2-DG+αKG cells ("oxygen transport" p_{adj} = 1,12e-06, "oxygen carrier activity" p_{adj} = 7,8e-08, "oxygen binding" p_{adj} = 1,3e-06, "erythrocyte differentiation" p_{adj} = 0,002). Markers associated with other hematopoietic functions were enriched ("B cell activation" p_{adj} = 0.01, "leukocyte mediated immunity" p_{adj} = 0.02, "macrophage activation" p_{adj} = 0.03, "platelet activation" p_{adj} = 0.04). The *in vitro* differentiation test also demonstrated that αKG reversed the effect of 2-DG on the differentiation capacity of the cells. The evolution

of cell populations with different cell surface marker combinations was similar to the control cells (**S9 Fig.**).

Contrary to AOA and 2-DG, αKG supplementation had no effect on the proliferation and cell surface marker distribution of the DON-treated cells during the first 96h (**Fig.6A**). αKG had only a slight effect on the pathway expression pattern of the DON-treated cells (**S8 Fig.**). As indicated earlier, DON-treated cells returned to normal proliferation and differentiation after the lag period. DON+αKG cells followed the same pattern (**Fig.6C and S9 Fig.**).

Finally, we examined the effect of αKG supplementation alone on the control cells. We observed no substantial effect neither on the cell proliferation or differentiation. Nevertheless, transcriptome analysis showed a slight effect on pathway activity (**S8 Fig.**).

In summary, αKG was able to compensate the short- and long-term effects of AOA and 2-DG. The rescue of the AOA-treated cells was the most spectacular. The partial inhibition of the transaminases strongly impacted all aspects of cellular physiology (proliferation, differentiation). These effects were fully reversed, but without fully reverting AOA's effect on gene expression. Less contrasted, but similar tendency was observed with 2-DG. Although αKG had no detectable effect on the control cells, it did influence their gene expression pattern also. The observations support the idea that not only energy metabolism, but many other essential physiological processes rely on αKG.

Discussion

Taken together, our data find that an early, partial and transitory inhibition of enzymes of the glucose or glutamine pathways generates perturbations of core cellular metabolism. These early perturbations trigger changes that interfere with the process of global chromatin opening typically occurring during the first 24 hours after the cells are stimulated. This interference is dependent on the type of metabolic stress. The gene expression profiles of cells are altered and show clear signs that the process of cell fate choice is affected. The long-term culture of the cells confirms that their differentiation capacity has been permanently modified by the early-stage transitory metabolic stress. Importantly, the response given by the cells to the transitory perturbation is heterogenous both at the level of the chromatin, gene expression and differentiation capacity.

A crucial question is whether the observed effects from inhibitors are linked to modifications in the cell fate choice process or result from the selective survival and amplification of a pre-existing minor cell population. The $CD34^+$ cell population is inherently heterogenous, and we used inhibitor concentrations close to the IC50 values. Therefore, the surviving cells exhibited greater resistance, likely due to their inherently more resistant metabolic state. Metabolic MS analysis was conducted on a bulk population, preventing conclusions at the single-cell level. However, time-lapse, cytometry, single-cell ATAC and RNA-seq analyses all provide information at the single-cell level. ATAC-seq revealed initial differences between control and treated cells approximately 12 hours after stimulation. By 24 hours, 16 different subsets of cells were identified using single-cell ATAC-seq chromatin

accessibility profiling. All four conditions were represented in all subsets in variable proportions. Previous studies [1,9] indicated that at 24 hours, these cells couldn't be clustered into distinct groups based on their gene expression patterns, suggesting that chromatin changes precede gene expression changes by several hours. Notably, at the time of analysis, these cells had not undergone division yet. Time-lapse microscopy revealed that the first division occurred in control and 2-DG cells 24 hours later, while in DON and AOA cells, it occurred only around 72 hours later. At this point, single-cell RNA-seq data clustering identified 17 different subsets of cells. Particularly, AOA cells exhibited a distinctly different gene expression pattern, forming separate clusters. Based on these observations, we think that although some selection occurs during the initial hours, the differences observed between the inhibitors cannot be solely explained by it. Instead, chromatin differences between cells appear before the first division of the cells surviving the initial shock. These differences then gradually evolve over the initial 96 hours. The inhibitors were removed at this point, and the cells primed by the different inhibitors were subsequently cultured under identical conditions. It is likely that cells exhibiting differential gene expression patterns possessed varying proliferation capacities, contributing to the observed evolution of cell populations as detected on days 7, 10, and 14.

Several important points arise from the observations. Restricting glucose access through partial inhibition of glycolysis by 2-DG reduces the capacity of the cells to survive and proliferate. However, presumably thanks to the availability of carbon and energy source provided by glutamine, the cells can rescue cellular functions. Glutamine is not only a carbon source; it is also the major source of nitrogen for nucleotide and amino-acid biosynthesis. Since glucose does not contain nitrogen, it cannot replace glutamine. Given that glutamine is non-essential, cells could potentially adapt to decreased external availability by redirecting their metabolism towards the utilization of alternative amino acids. The time required for the metabolic adaptation and recovery of the biosynthetic capacity from altered resources may explain the long lag before the first division of the DON- and AOA-treated cells. Nevertheless, there is a notable difference between the effect of DON and AOA. The latter impacted stronger the physiology of the surviving cells and they never recover completely their capacity to grow and divide. Inhibition of the transaminases in the $CD34^+$ cells appear therefore more difficult to compensate by alternative strategies than the inhibition of the upstream step of the glutamine utilization. Indeed, transaminases catalyze a key step that links the glutamine metabolism to the central energy metabolism through the deamination of glutamate resulting in αKG. AOA also inhibits the malate-aspartate shuttle and block the electron flow between the cytoplasm and the mitochondria resulting in reduced ATP synthesis. Aspartate was indeed shown to be essential for hematopoietic cell differentiation and entirely dependent on cell-autonomous synthesis [23]. Importantly, external αKG could fully compensate the effect of transaminase inhibition by AOA showing that the effect of AOA is essentially conveyed by this intermediate of the TCA cycle. αKG is well known for its role as a substrate of DNA and histone demethylating enzymes [24,25]. It's involvement in epigenetic mechanisms is likely to be the key to its role in stem cell function and cell differentiation [26–29]. The role of αKG in the self-renewal and differentiation of hematopoietic stem cells is also widely recognized [30]. The disparity in chromatin impact between AOA and DON, along with

AOA's responsiveness to αKG, might reside in the configuration of the glutamine metabolic pathway. DON's inhibition effects on αKG production can be more readily offset by other amino acids, given that glutamine is a non-essential amino acid. This aligns with the observed recovery of surviving cells after an initial setback, where they subsequently resume their proliferation and differentiation following a brief lag period. Conversely, compensating for the inhibition caused by AOA is more challenging due to the direct involvement of transaminases in αKG production.

Cell differentiation is typically explained as a process driven by the dynamics of gene regulatory networks [31–34]. This description is undoubtedly incomplete because it dismisses the required bioenergetic component of the process. It is separately understood that the cell's survival is intricately linked to the continuous flow of energy. Yet, this is rarely included in the explanatory scheme, nor has this been considered as a driver of cell state/fate changes. The energy flow is ensured by the stepwise oxidation of the carbon source molecules taken up from the environment with the concomitant conversion of the chemical energy into small high energy metabolites ready to be used in biochemical reactions. Since the availability of the carbon sources is out of the cell's control, their response to a decreased energy supply is limited to switching to a new energy source. This transition corresponds to a differentiation process. Since metabolic adaptation is the absolute requirement for the survival of every cell, the insufficiency of the bioenergetic resources alone would represent a universal stimulation for differentiation. Although the biochemical links between the nutrient availability, key metabolites, epigenetic mechanisms, and cell differentiation are now well recognized, the exact character of this connection remains unclear. As recently formulated: "The observation that TCA cycle metabolites can control αKG-dependent dioxygenases and cell fate raises major questions, including how a nonspecific signal such as TCA cycle intermediate abundance can lead to a specific outcome in cell fate." [35]. From our data in this study, we infer that the *nonspecific* metabolic stress acts as a primary "activating signal" required to generate a variety of nonspecific, dynamically fluctuating chromatin- and gene expression responses. This can represent the multilineage primed state in hematopoietic cells [36–38]. Indeed, similar transcription responses have been observed in all the other cell differentiation models examined [39]. This exploratory dynamic generates variants with distinct gene expression patterns that can restore the energy flux by sampling any alternative metabolic sources available in the environment. Different cells can reach different "solutions" i.e. different phenotypic states in the same environment and form a cellular ecosystem that supports metabolic cooperation but not necessarily free of competition. Such cooperative cellular setups that characterize the multicellular organisms are very well known in the unicellular world [40–43]. The specific outcome of the nonspecific stress response also relies on intracellular factors commonly referred to as cellular- or epigenetic memory. The degree of chromatin opening in response to metabolic stress also depends on the nature and density of pre-existing repressive modifications reflecting the life history of the cell. Separately, it is worth mentioning that, although not considered in this paper, post-translational modifications of many cellular proteins unrelated to chromatin but dependent on the same sentinel metabolite substrates also could potentially contribute to the cellular memory process.

It is becoming increasingly popular to consider cell differentiation as a process of selective stabilization of gene expression profiles generated by spontaneous stochastic variation of gene transcription analogous to the process of evolution [44–48]. Others compared differentiation to a “learning process” [49,50]. The initial theory has been further developed by including energy metabolism as an essential part of the process [51,52]. According to possible scenarios based on these considerations metabolic stress induces a nonspecific and highly variable response. Extrinsic and intrinsic constraints and contingencies selectively stabilize those responses that allow better survival. The epigenetic mechanisms stabilize and ensure the transmission of the cellular state until a next metabolic stress. Although speculative, the observations presented in this paper provide arguments in favor of this theoretical model and integrate our previous knowledge on the underlying molecular mechanisms in a coherent way. They demonstrate, using a widely used experimental model, that a significant metabolic stress may be the initial event, immediately followed by global chromatin decompaction. The exact nature of the metabolic stress and the cells intrinsic properties together canalize the chromatin modifications that generate differences in gene expression at a later stage. This is sufficient to impact the subsequent cell fate trajectories even if the initial metabolic stress has ceased.

There are many observations making causal link between metabolism and cell differentiation or stem cell properties in the hematopoietic and other cellular systems [16,18,29,53]. Typical explanations for the above link each observed effect to very specific molecular mechanisms acting in specific circumstances [54,55]. Our model provides a more generalizable explanation for all cases. In addition, we can also speculate on an evolutionary perspective for cell differentiation. In fact, multicellularity and cell differentiation appeared multiple times during evolution [56,57], before specific molecular mechanisms emerged, suggesting that their role in the process of cell differentiation could be supportive. A popular view of cell differentiation is to consider the stable cell phenotype as an attractor in the multidimensional Waddington-type epigenetic landscape defined by the gene regulatory network [32–34,58]. Differentiation is seen as a transition between two attractors. Our model integrates this vision where the attractors are defined, in addition to the gene regulatory network, by the metabolic fluxes and the influence they have on the dynamics of the epigenetic chromatin states. As a result, the Waddington landscape is not simply determined by the intrinsic properties of the gene network, but becomes a dynamic process, resulting from the interactions between intrinsic and extrinsic constraints.

Materials and methods

Ethics statement

Human umbilical cord blood was collected from placentas and/or umbilical cords from anonymous donors obtained from AP-HP, Hôpital Saint-Louis, Unité de Thérapie cellulaire, CRB-Banque de Sang de Cordon, Paris, France (Authorization number : AC-2016-2759) or from Centre Hospitalier Sud Francilien, Evry, France, in accordance with international ethical principles and French national law (bioethics law n° 2011–814) under declaration N° DC-201-1655 to the French Ministry of Research and Higher Studies.

Cell culture

Human $CD34^+$ cells were isolated from umbilical cord blood of anonymous healthy donors. After an erythrocytes depletion step using Dextran from *Leuconostoc* spp. (Sigma Aldrich, M_r 450000-650000), cells were separated by density centrifugation using Ficoll (Biocoll, Merck Millipore). The mononuclear fraction was collected and enriched in $CD34^+$ by immunomagnetic beads using manual MACS® system (Miltenyi Biotech). After collection, enriched $CD34^+$ cells were frozen in a cryopreservation medium containing 90% of fetal bovine serum (Eurobio) and 10% of dimethylsulfoxide (Sigma) and stored in liquid nitrogen.

After thawing, cells were cultured at 37°C in a humidified 5% CO_2 incubator in prestimulation medium supplemented with h-Flt3-L (50ng/mL), h-IL3 (10ng/mL), h-SCF (25ng/mL) and h-TPO (25ng/mL) as previously described [1,9]. Metabolic inhibitors were added to the medium at their IC50 concentration determined experimentally. 6-Diazo-5-oxo-L-norleucine (DON) was used at final concentration of 2,5µM (Sigma Aldrich, ref. D2141). 2-Desoxy-D-glucose (2-DG) was used at final concentration of 1mM (Sigma Aldrich, ref. D3179). Aminooxyacetic acid (AOA) was used at final concentration of 1,9mM (Sigma Aldrich, ref. C13408). Some rescue experiments were performed with addition of dimethyl α-ketoglutarate in the inhibitor-medium mix at final concentration of 5mM (Sigma Aldrich, ref. 349631). Inhibitors were stored according to the supplier's recommendations.

Metabolic inhibitors were added to the culture medium at time point 00h of the experiments. For all time points less than 96hrs of culture and for the time-lapse experiments, no medium change occurred. Nonetheless, the cytometry experiment on long term cultures involved some experimental adjustments. After 96hrs of culture with inhibitors as described above, the medium was changed, and all cells were cultured in optimized prestimulation medium for long term differentiation without inhibitors. Four more cytokines were added to the medium to allow unrestricted differentiation of the cells towards hematopoietic lineages: 1U h-EPO, 10 ng/mL h-IL6, 20 ng/mL h-GM-CSF, 20 ng/mL h-G-CSF final concentration (PeproTech). Half of the medium was removed every two days and cell density was adjusted to 500 000 cells/mL with fresh medium (or 300 000 cells/mL before weekends).

Time-lapse microscopy

The time-lapse microscopy protocol was previously described [9,59,60]. Cells were cultured in a four compartments dish (Ibidi Hi-Q4) combined with PDMS microgrid array (Microsurfaces). Each compartment contained a different condition (control medium or metabolic inhibitors) allowing all the conditions to be assessed parallelly in the same experiment. Time-lapse acquisitions were performed with the inverted microscope Olympus IX83 combined with a thermostatic culture chamber from CISA platform (CRSA, Paris, France). Images were acquired every two minutes using a 10X objective for 7 days. Microwells containing less than 8 cells in the first image were considered in the analysis to allow cell tracking.

Cytometry on short-term culture with generational tracking

After thawing, $CD34^+$ cells of three independent healthy donors were labeled separately using the CellTrace™ Violet (CTV) Proliferation Kit (Invitrogen) to allow tracking of multiple generations with dye dilution. A sample of those parental generation cells were used to measure fluorescence intensity at time point 00h. The other cells were incubated according to the conditions described earlier. At 96hrs, cells were harvested and labeled using CD133-APC (Miltenyi Biotech, clone AC133, dilution 1:50) and CD34-PE (Miltenyi Biotech, clone AC136, dilution 1:10) cell-surface antibodies after a non-specific sites' saturation step with Gamma Immune (Sigma Aldrich, dilution 1:2). Isotype controls (Miltenyi Biotech), Versacomp compensation beads (Beckman Coulter) and negative controls were used for subsequent gating strategy. Viability was controlled using 7-Aminoactinomycine D marker (Invitrogen). Fluorescence intensity of CTV and antibodies was measured with the SP6800 cytometer (Sony) from ImCy platform (Généthon, Evry, France).

Cytometry on long-term cultures

Cytometry results represent at least three biological replicates for each time point on long-term culture and were obtained from a combination of seven experiments with mixes of ten independent healthy donors. Cells were cultured in prestimulation medium with or without metabolic drugs and αKG during the firsts four days and then in optimized prestimulation medium without inhibitor or αKG as described before. Sample of cells were collected at day 4, 7, 10 and 14 to be analyzed by flow cytometry on CytoFLEX V5-B5-R3 Flow Cytometer (Beckman Coulter). After a saturation step with Gamma Immune (Sigma Aldrich, dilution 1 :2), cells were labeled with antibodies detecting the following cell-surface markers: CD133-APC (Biolegend, clone 7, dilution 1:20), CD19-PECy7 (Biolegend, clone HIB19, dilution 1:80), CD36-PerCPCy5.5 (Biolegend, clone 5-271, dilution 1:40), CD45-BV421 (Biolegend, clone HI30, dilution 1:80), CD15-APCFire750 (Biolegend, clone W6D3, dilution 1:80), CD14-BV785 (Biolegend, clone M5E2, dilution 1:80), CD41-BV605 (Biolegend, clone HIP8, dilution 1:40) and Zombie Aqua™ fixable viability dye (Biolegend, dilution 1:200). For each experiment, compensation beads (Miltenyi, ref. 130-097-900) were used for positive monolabeling controls and unmarked cells for negative controls.

Mass spectrometry

Cells of at least two independent healthy donors were mixed for each experiment and cultured during 24 hours with or without the inhibitors then collected for the extraction of metabolites. Cell suspensions were adjusted to 8mL final volume and mixed with 42mL of quenching solution (60% (vol/vol) methanol, 0.85% (wt/vol) ammonium bicarbonate, completed with milli-Q water and pH adjusted at 7.4) cooled at -40°C. After centrifugation at 1000g during 1min and removal of the quenching solution by aspiration cell pellets were re-suspended in extraction buffer (80% ethanol) and vortexed vigorously to release all the intracellular metabolites. After another centrifugation and vortexing steps, supernatants were collected and centrifuged at 15 000g for 5min. Supernatants were collected and dried using Speed Vacuum Concentrator 5301 (Eppendorf, ref.530101197, 230 V, 1.4 A, 50Hz, 310 W) for 3 to 5hrs. Metabolite extracts were kept at minus 80 degrees before subsequent steps. Subsequently, targeted metabolites from distinct pathways (amino acids, tricarboxylic cycle, sugar phosphates) were measured either with or without chemical derivatization, as described in detail earlier [19], using a QTRAP 6500 LC/MS/MS based platform (ABSciex).

Bulk ATAC-seq

5000 living cells of three independent healthy donors were sorted by FACS (Beckman Coulter) based on 7-AAD labeling. For library preparation we used the Fast ATAC-seq protocol optimized for blood cells with minor modifications, as previously described [1]. After a quality control using Bioanalyzer (Agilent), libraries were sent to the CNRGH (CEA, Evry, France) for sequencing (NextSeq Illumina).

10X Single-cell ATAC-seq

After 24 hours of culture of a mixed cell suspension from six healthy donors, dead cells were removed using Dead Cell Removal Kit (Miltenyi Biotech). Samples were brought to the technical platform of the IMAGINE Institute (https://www.institutimagine.org/en) which performed the experiment and raw data processing. Nuclear isolation was carried out following 10X Genomics protocol (CG000124) and nuclei were counted using Luna automated Cell Counter (Logos). Libraries were prepared using Chromium Next GEM Single Cell ATAC Reagent Kit v1.1 (10X Genomics, protocol CG000209) from around 15 000 single nuclei for each condition. After the loading step on the microfluidic device, between 4000 and 6000 nuclei per sample were successfully encapsulated for further analysis at the single-cell level. Following a quality control checkup with Qubit Fluorometer, libraries were then sequenced on Flowcell S1 on a NovaSeq 6000 (Illumina).

10X Single-cell RNA-seq – CITE-seq

Pools of cells from seven independent donors were cultured during 96 hours with or without inhibitors and αKG as described above. Cells were harvested and dead cells were removed

using Dead Cell Removal Kit (Miltenyi Biotech). Single-cell RNA-seq with feature barcoding technology for cell surface protein (CITE-seq) was then carried out following the Chromium Next GEM Single Cell 3' protocol for v3.1 reagents from 10X Genomics (CG000206 Rev D) and TotalSeq™-A Antibodies and Cell Hashing protocol from Biolegend (available online at https://www.biolegend.com/en-gb/protocols/totalseq-a-antibodies-and-cell-hashing-with-10x-single-cell-3-reagent-kit-v3-3-1-protocol). Cell hashing with hashtag oligos (HTOs) allows to mix different samples together after staining and though to reduce the number of required chips for sequencing. Multiomic cytometry involves cell staining with antibody derived tags (ADTs) to identify targeted cellular surface epitopes. Consequently, cells were first labelled with cocktails of HTOs (Biolegend, TotalSeq™ A0251 anti-human hashtag1 and TotalSeq™ A0252 anti-human hashtag2) and ADTs antibodies (Biolegend, TotalSeq™ A0126 anti-human CD133 and TotalSeq™ A0054 anti-human CD34) used at 1M/mL as suggested, after saturation of non-specific sites with Humain TruStain FCX FC Blocking Reagent (Biolegend). Then, around 20 000 labelled cells per sample were loaded into the microfluidic device to obtain between 5000 and 10 000 encapsulated cells in GEMs. Barcoded cDNAs were amplified and sent to the GENOM'IC platform (Cochin, Paris, France) for libraries preparation and sequencing on NextSeq™ 500/550 (Illumina).

Bioinformatic analysis

Time-lapse analysis

Time-lapse images were analyzed using *ImageJ* software (Rasband, W.S., *ImageJ*, U. S. National Institutes of Health, Bethesda, Maryland, USA, https://imagej.nih.gov/ij/). For proliferation and viability, cell tracking was performed manually using the *ImageJ* "Cell Counter" plugin. For each frame, living and dead cells were counted and events like cell divisions were recorded. The count tables were then exported in .csv format to be graphically analyzed using custom R scripts (v3.6.0) with ggplot2 package (v3.2.1). More than 150 microwells with one to eight initial cells were analyzed. For morphology tracking, a semi-automatic method in three steps was developed. First, images were automatically segmented with deep learning based CellPose algorithm [61] and errors were removed with a homemade macro built on *ImageJ*. Then, cells tracking was performed with the Lineage Mapper *ImageJ* plugin. 50 to 100 cells were successfully tracked per condition. A unique identifier was attributed to individual cells based on segmented images and conserved along the cell cycle. At each division, identifier was renewed with two others for daughter cells. This method allows for cell migration and division tracking and measuring cell cycle duration. Cell features over time (coordinates, area, perimeter...) were exported in a .csv file using another custom *ImageJ* macro. Finally, the table was used in R (v4.2.1) to compute roundness, cell cycle duration and morphological switch rate (as described in [9]) and to generate plots with ggplot2 package.

Cytometry analysis

Flow cytometry .fsc files were analyzed with Kaluza software (v2.1). For short-term culture experiments, emission wavelengths of the chosen fluorochromes were sufficiently distant to not require compensation step. Gates were manually adjusted using positive and negative controls and generations were identified based on the CTV fluorescence intensity histogram. Proliferation indexes were calculated as described in [62] with the following formula : $\frac{\sum_0^i N_i}{\sum_0^i \frac{N_i}{2^i}}$ where i is the generation number and Ni is the number of events in generation i. For long-term culture experiments, a compensation matrix was automatically created using the monolabeled samples from all experiments at all time points. Manual checking of the obtained matrix and adjustments were next performed. Then, gates were placed using FMO data and unlabeled samples from each experiment. One gating protocol was established for each time point. Finally, compensation matrix and gating protocols were applied on the samples and statistical tables for each marker and combinations of markers were exported in .csv format to be graphically plotted with R software (v4.3.0) and ggplot2 package (v3.4.2).

Mass spectrometry analysis

Results from the nine conducted experiments were merged into a common table using R (v4.3.1). Data were then normalized by the initial number of cells used for the experiments before the metabolite extraction. Samples showing excessive variations between technical replicates were excluded from the dataset. For each metabolite, the mean values of the technical replicates were used for further analysis. The values obtained in each experimental condition were normalized to their respective controls.

Bulk ATAC-seq analysis

Raw sequence data were cleaned and aligned on hg19 assembly by the CNRGH bioinformatic facility using common tools as: trimmomatic (v0.32), bowtie2 (v2.4.1), samtools (v1.4), macs2 (v2.1.1), picard (v1.138) and bedtools (v.2.29.2). Output .bam files were retrieved and handled with a custom snakemake (v7.25.0) workflow. First, the three biological replicates of each time point and condition were pooled together with samtools merge function (v1.11). Others samtools functions were then used to index the files, extract quality control values and count read number. No sample needed to be excluded based on quality control statistics. Using the samtools view function we performed down sampling to the smallest number of reads detected in the cohort (80 000 000 reads). A new peak calling was conducted on downsampled .bam files using the macs2 callpeak tool (v2.2.7.1) with the following parameters: <-f BAMPE -g hs -B –broad –broad-cutoff 0.1>. Files were used as inputs in custom R scripts (v4.2.1). Readcount matrices were created for each merged sample with featureCounts function (Rsubread v2.4.0) and a threshold on the minimum number of reads per peak was applied to remove technical background noise. Only peaks with 10 or more reads were kept for further analysis. Finally, Granges objects were created with GenomicRanges package (v1.42.0) to be used in downstream analysis. To compare the accessibility profiles between different conditions and time points, a common list of regions

was defined with Reduce:union function from GenomicRanges. Differential accessibility analysis was then performed following DEseq2 documentation (v1.38.3) and PCA was carried out with prcomp function from stats base package. Plots were drawn with ggplot2 (v3.4.2).

Single-cell ATAC-seq analysis

Fastq files generated as sequencing output were cleaned and aligned to the hg38 reference genome by the bioinformatic facility of IMAGINE Institute using Cell Ranger software (10X Genomics, pipeline version: cellranger-atac-2.0.0). Count matrices were imported into R (v4.2.1) and integrated into a Chromatin Assay object using Seurat (v4.1.3) and Signac (v1.9.0) packages. Following the vignette's packages, QC metrics were computed to assess data quality and filter out peaks and cells of bad quality. Only cells with at least 200 peaks detected, nucleosome signal <2, blacklist ratio <0.05, TSS enrichment >2, number of fragments overlapping peaks between 3000 and 50 000 and minimum 50% of total fragments fallen within ATAC-seq peaks were kept. Moreover, only peaks detected in at least 100 cells were retained and nonstandard chromosomes were removed from the analysis. To allow comparison between the different conditions, a common set of peaks across the whole dataset was extracted with reduce function from Signac package and Chromatin Assay objects were merged. TF-IDF normalization followed by singular value decomposition (SVD) were performed on the top features shared by more than 90% of the cells. Dimensions 2 to 50 of LSI reduction were used for dimensional reduction and clustering analysis. Louvain Algorithm was used for clustering with resolution 0,25. As the total cell counts differ across conditions, a normalization procedure was required to be able to compare the cells' distribution in clusters across conditions. Cells' numbers in each cluster were divided per the initial number of cells of the concerned condition and multiply by 1000. Gene ontology analysis was performed using org.Hs.eg.db (v3.16.0) and clusterProfiler (v4.6.2) packages. Most of the plots were drawn with ggplot2 (v3.4.2) package.

Comparison bulk and single cell ATAC-seq

To compare the bulk ATAC-seq and the scATAC-seq samples at 24h, aligned reads from single cell experiment were shifted from hg38 to hg19 reference genome as described in [1].

Single-cell RNA-seq analysis

Demultiplexing and raw data alignment on hg38 genome were conducted by the bioinformatic facility of GENOM'IC platform with Cell Ranger software (10X Genomics, pipeline version: cellranger-6.0.1, *cellranger multi* function). Seurat Objects were created from Cell Ranger count matrices with Seurat package (v4.3.0) for downstream analysis on R (v4.2.1). Cumulative quality control filters were applied on the dataset to keep only good quality information. Inasmuch as the GEMs formation is not free from a certain error's percentage, a filter on the minimum and maximum number of genes detected in a cell to be considered as a real one was applied to remove empty GEMs and doublets. Only cells with

1000 to 6500 detected genes were kept for further analysis. Moreover, cells presenting a high percentage of mitochondrial RNA and a low percentage of ribosomal RNA are either dead or dying. Thus, another filter was applied to keep cells with less than 25% of mRNA and more than 5% of rRNA. The 13 mitochondrial genes were also removed from the count matrices. Finally, only genes detected in more than 3 cells (among the 5000 analyzed) were retained. After this cleaning step, normalization of the RNA assay was performed with SCTransform algorithm (package sctransform v0.3.5) with *variable.features.n* and *ncells* parameters set to NULL and threshold on residual variance at 1,3. Meanwhile, the ADT assay from CITE-seq measurement was normalized across cells with the centered log ratio method (CLR) as advised on Seurat multimodal data vignette. After confirmation that batch effect correction was not required, data from all conditions and experiments (control, inhibitors and rescue) were combined into a single Seurat Object. Control samples from multiple experiments were shuffled and further considered as one. Linear dimensional reduction with PCA was then performed and dimensions 1 to 40 were kept for later UMAP analysis and cluster identification. Using SLM algorithm [63] and with the help of clustree package (v0.5.0), cluster resolution 0.6 was selected leading to 17 cells clusters. As for the scATAC-seq analysis, cell's numbers were normalized by the total number of cells per condition. Downstream analysis was carried out using ggplot2 (v3.4.2) and Seurat functions for most of the plots. The FindAllMarkers function from Seurat was used to extract the top 20 positive markers for each cluster. Thresholds on adjusted pvalue (<0.05) and percentage of cells expressing the markers (pct.1 – pct.2 > 0.25) were applied on the list before creating heatmap with DoHeatmap function. Membrane protein groups of expression based on CITE-seq results were defined using the kmeans function from stats base package. Gene Ontology analysis on differentially expressed genes between conditions was performed with org.Hs.eg.db (v3.15.0) and clusterProfiler (v4.4.4) packages. Two methods were used extract lists of differentially expressed genes. On one hand, visual outliers were identified on scatter plots of average gene expression. For each gene, average UMI number of both the control and perturbed cells was calculated and reported on the x and y axis of the plot. Arbitrary thresholds at +/-0.5 were set, highlighting genes that exhibit high responses (upregulation or downregulation) to the metabolic perturbation. On the other hand, another list of positive and negative markers was identified with the FindMarkers function from Seurat package (test.use = "wilcox", logfc.threshold = 0.25, p_val_adj<0.05). Both lists were used for Gene Ontology analysis. The pathways analysis was performed with ReactomeGSA (v1.10.0) on normalized gene expression to identify pathway level enrichment between conditions. Prior to it, a list of interesting pathways had been extracted from ReactomeContentService4R (v1.2.0) database.

Conflict of interest statement

The authors have declared that no competing interest exists.

Funding

This work was supported by EPHE grant (11REC/BIMO to AP), ANR grant (ANR-17CE12-0031-01 «SinCity » to AP). The funders had no role in study design, data collection and analysis, decision to publish, or preparation of the manuscript.

Data accessibility statement

Data are available under the NCBI GEO accession number GSE243006. This accession number regroups three subseries of data: GSE243003 with bulk ATAC-seq data, GSE243004 with scATAC-seq data and GSE243005 with scRNA-seq and CITE-sed data.

Acknowledgments

The authors are grateful to Romain Morichon, Daniel Stockholm and Jérémie Cosette for their help with time-lapse recording, to Peggy Sanatine for providing training in the use of the cytometer SP6800 for CTV cytometry and to Thierry Jaffredo for his support during the use of the Chromium 10X device for scRNA-seq experiment. We also acknowledge the use of instruments and resources at the Mass spectrometry facility at inStem and NCBS. The authors would like to extend special thanks to Camille Baey from Biolegend for her assistance, valuable advice, and time dedicated for the setup and optimization of the long-term cytometry panel. Moreover, we would like to thank all the members of the platforms that performed sequencing and bioinformatic preprocessing of the NGS data: Brigitte Izac and Benjamin SaintPierre from GENOM'IC platform, Marine Luka and Francesco Carbone from IMAGINE platform and Sophie Chantalat from CNRGH. The authors are also grateful to the mothers and the staff of the Centre Hospitalier Sud Francilien and AP-HP Hôpital Saint-Louis for umbilical cord blood samples. We are grateful to Prof. Takuya Imamura for his valuable comments and suggestions.

Author Contributions

Conceptualization : Andras Paldi
Data curation : Laëtitia Racine
Formal analysis : Laëtitia Racine, Romuald Parmentier, Sunil Laxman
Funding acquisition : Andras Paldi
Investigation : Laëtitia Racine, Romuald Parmentier, Julie Chhun, Shreyas Niphadkar
Methodology : Laëtitia Racine, Romuald Parmentier, Sunil Laxman
Software : Laëtitia Racine
Supervision : Andras Paldi
Validation : Laëtitia Racine, Romuald Parmentier, Sunil Laxman
Visualization : Laëtitia Racine
Writing – original draft : Laëtitia Racine, Andras Paldi, Romuald Parmentier, Sunil Laxman
Writing – review & editing : Laëtitia Racine, Andras Paldi, Romuald Parmentier, Sunil Laxman

Figures

Fig 1

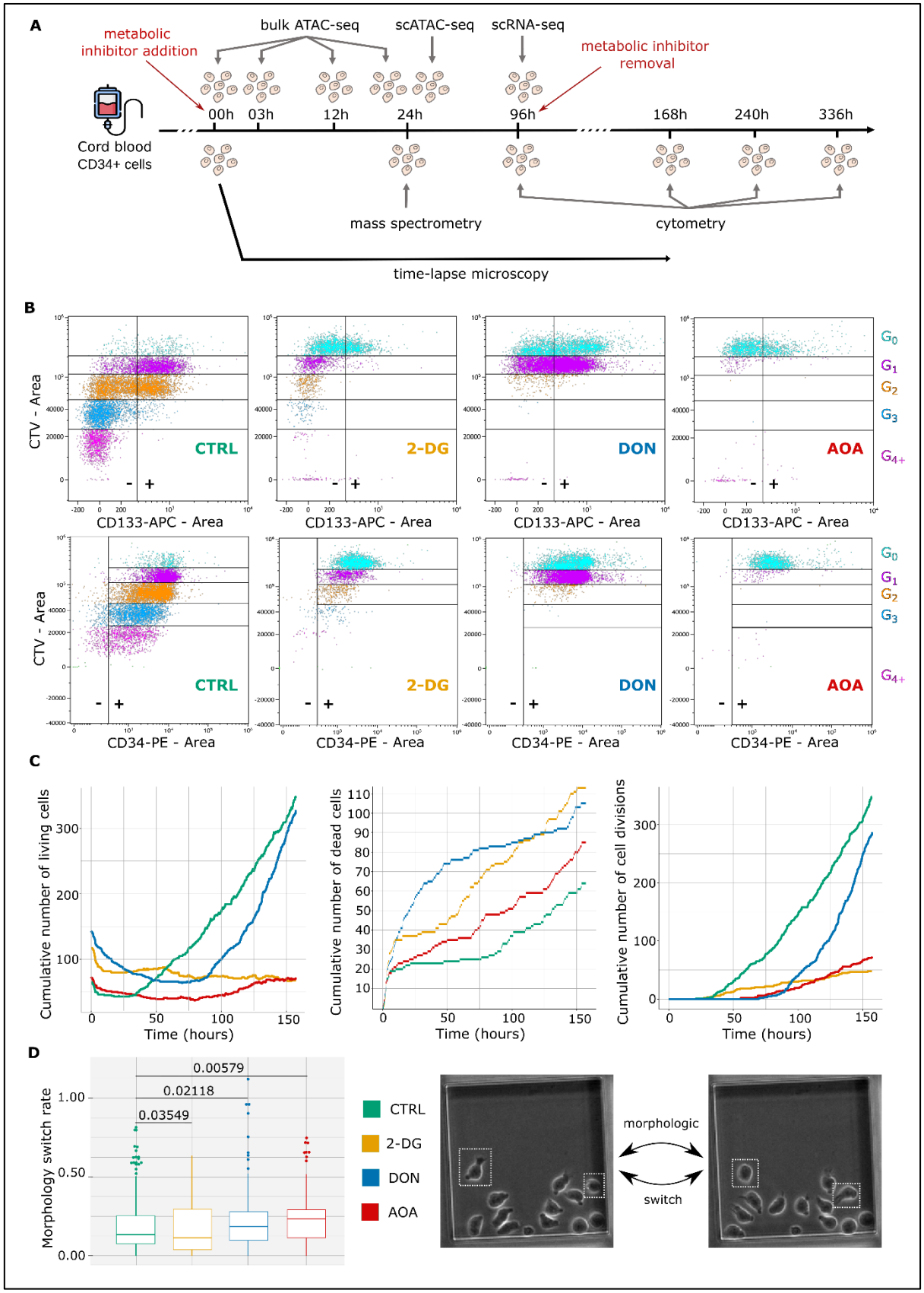

Fig 2

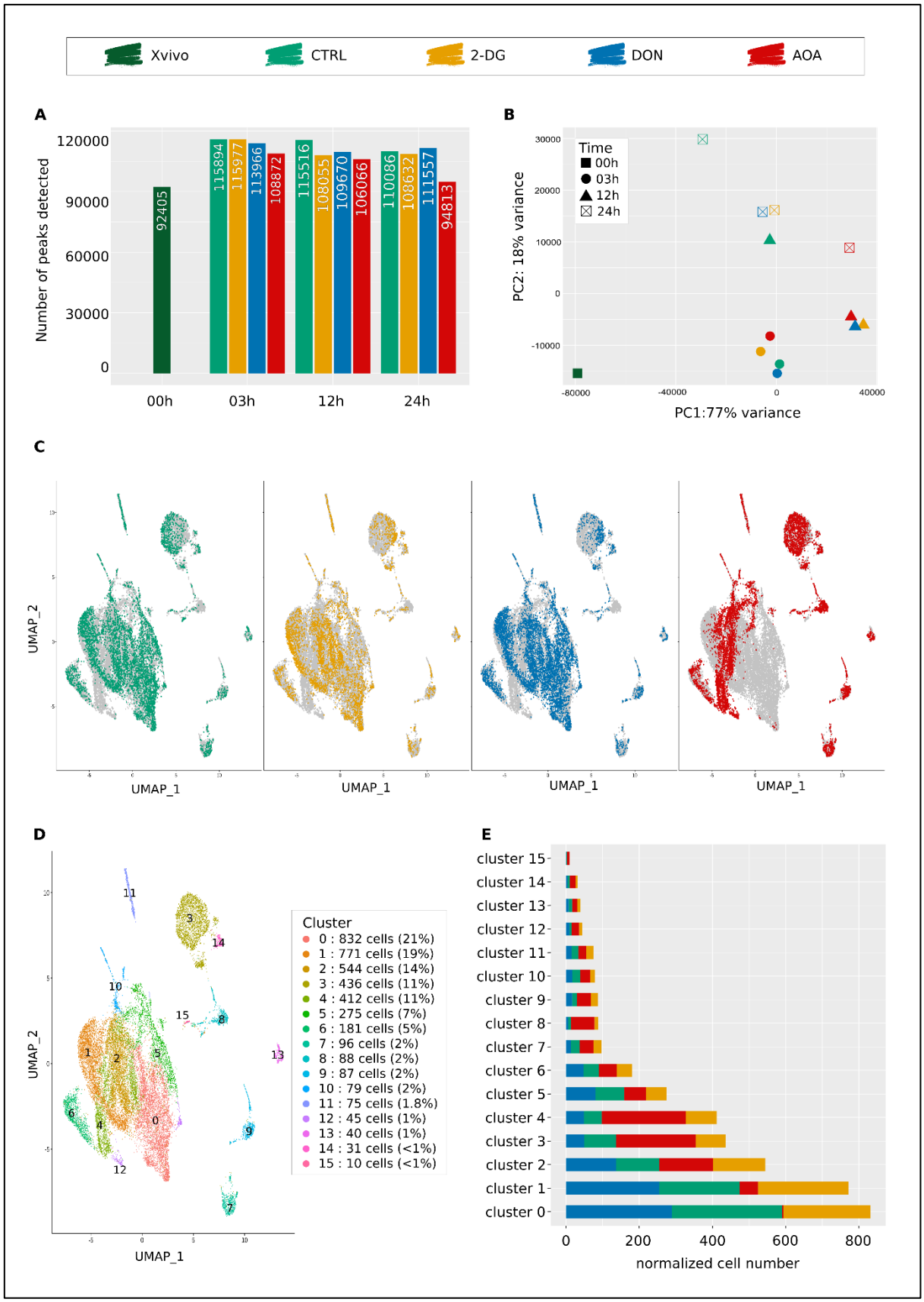
Xvivo
CTRL
2-DG
DON
AOA
A
Number of peaks detected
120000
90000
60000
30000
0
92405
115894
115977
113966
108872
115516
108055
109670
106066
110086
108632
111557
94813
00h
03h
12h
24h
B
PC2: 18% variance
PC1:77% variance
Time
00h
03h
12h
24h
C
UMAP_2
UMAP_1
D
Cluster
0 : 832 cells (21%)
1 : 771 cells (19%)
2 : 544 cells (14%)
3 : 436 cells (11%)
4 : 412 cells (11%)
5 : 275 cells (7%)
6 : 181 cells (5%)
7 : 96 cells (2%)
8 : 88 cells (2%)
9 : 87 cells (2%)
10 : 79 cells (2%)
11 : 75 cells (1.8%)
12 : 45 cells (1%)
13 : 40 cells (1%)
14 : 31 cells (<1%)
15 : 10 cells (<1%)
E
cluster 15
cluster 14
cluster 13
cluster 12
cluster 11
cluster 10
cluster 9
cluster 8
cluster 7
cluster 6
cluster 5
cluster 4
cluster 3
cluster 2
cluster 1
cluster 0
0
200
400
600
800
normalized cell number

Fig 3

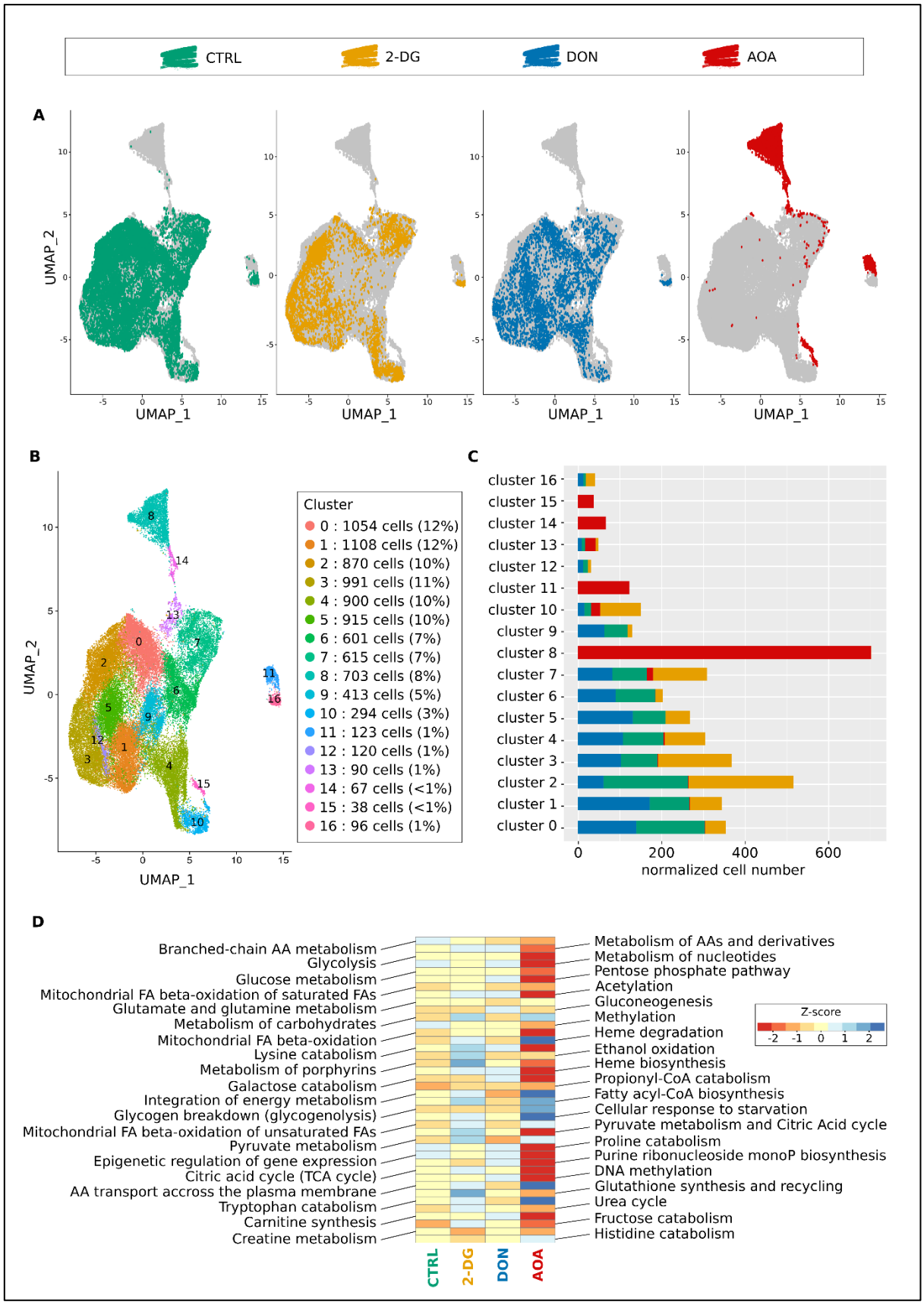
CTRL
2-DG
DON
AOA
A
UMAP_2
UMAP_1
B
Cluster
0 : 1054 cells (12%)
1 : 1108 cells (12%)
2 : 870 cells (10%)
3 : 991 cells (11%)
4 : 900 cells (10%)
5 : 915 cells (10%)
6 : 601 cells (7%)
7 : 615 cells (7%)
8 : 703 cells (8%)
9 : 413 cells (5%)
10 : 294 cells (3%)
11 : 123 cells (1%)
12 : 120 cells (1%)
13 : 90 cells (1%)
14 : 67 cells (<1%)
15 : 38 cells (<1%)
16 : 96 cells (1%)
C
cluster 16
cluster 15
cluster 14
cluster 13
cluster 12
cluster 11
cluster 10
cluster 9
cluster 8
cluster 7
cluster 6
cluster 5
cluster 4
cluster 3
cluster 2
cluster 1
cluster 0
normalized cell number
D
Branched-chain AA metabolism
Glycolysis
Glucose metabolism
Mitochondrial FA beta-oxidation of saturated FAs
Glutamate and glutamine metabolism
Metabolism of carbohydrates
Mitochondrial FA beta-oxidation
Lysine catabolism
Metabolism of porphyrins
Galactose catabolism
Integration of energy metabolism
Glycogen breakdown (glycogenolysis)
Mitochondrial FA beta-oxidation of unsaturated FAs
Pyruvate metabolism
Epigenetic regulation of gene expression
Citric acid cycle (TCA cycle)
AA transport accross the plasma membrane
Tryptophan catabolism
Carnitine synthesis
Creatine metabolism
Metabolism of AAs and derivatives
Metabolism of nucleotides
Pentose phosphate pathway
Acetylation
Gluconeogenesis
Methylation
Heme degradation
Ethanol oxidation
Heme biosynthesis
Propionyl-CoA catabolism
Fatty acyl-CoA biosynthesis
Cellular response to starvation
Pyruvate metabolism and Citric Acid cycle
Proline catabolism
Purine ribonucleoside monoP biosynthesis
DNA methylation
Glutathione synthesis and recycling
Urea cycle
Fructose catabolism
Histidine catabolism
Z-score
CTRL
2-DG
DON
AOA

Fig 4

CTRL
2-DG
DON
AOA
A
Proportion of living cells
D4
D7
D10
D14
B
CD133+
CD14+
CD15+
CD19+
CD36+
CD41+
CD45+
Proportion of positive cells

Fig 5

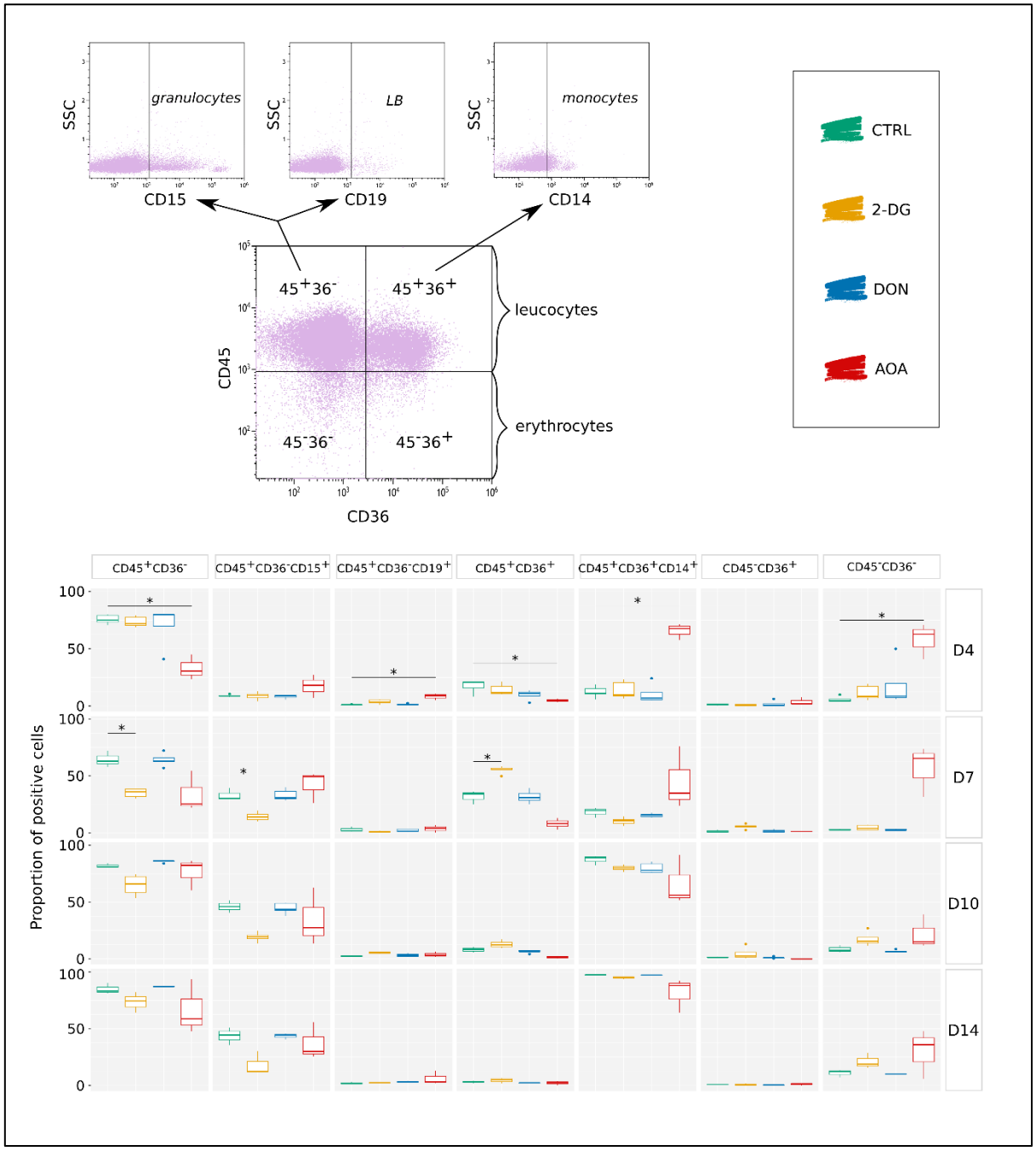
SSC
granulocytes
CD15
SSC
LB
CD19
SSC
monocytes
CD14
CD45
CD36
45+36-
45+36+
leucocytes
45-36-
45-36+
erythrocytes
CTRL
2-DG
DON
AOA
CD45+CD36-
CD45+CD36-CD15+
CD45+CD36-CD19+
CD45+CD36+
CD45+CD36+CD14+
CD45-CD36+
CD45-CD36-
Proportion of positive cells
D4
D7
D10
D14

Fig 6

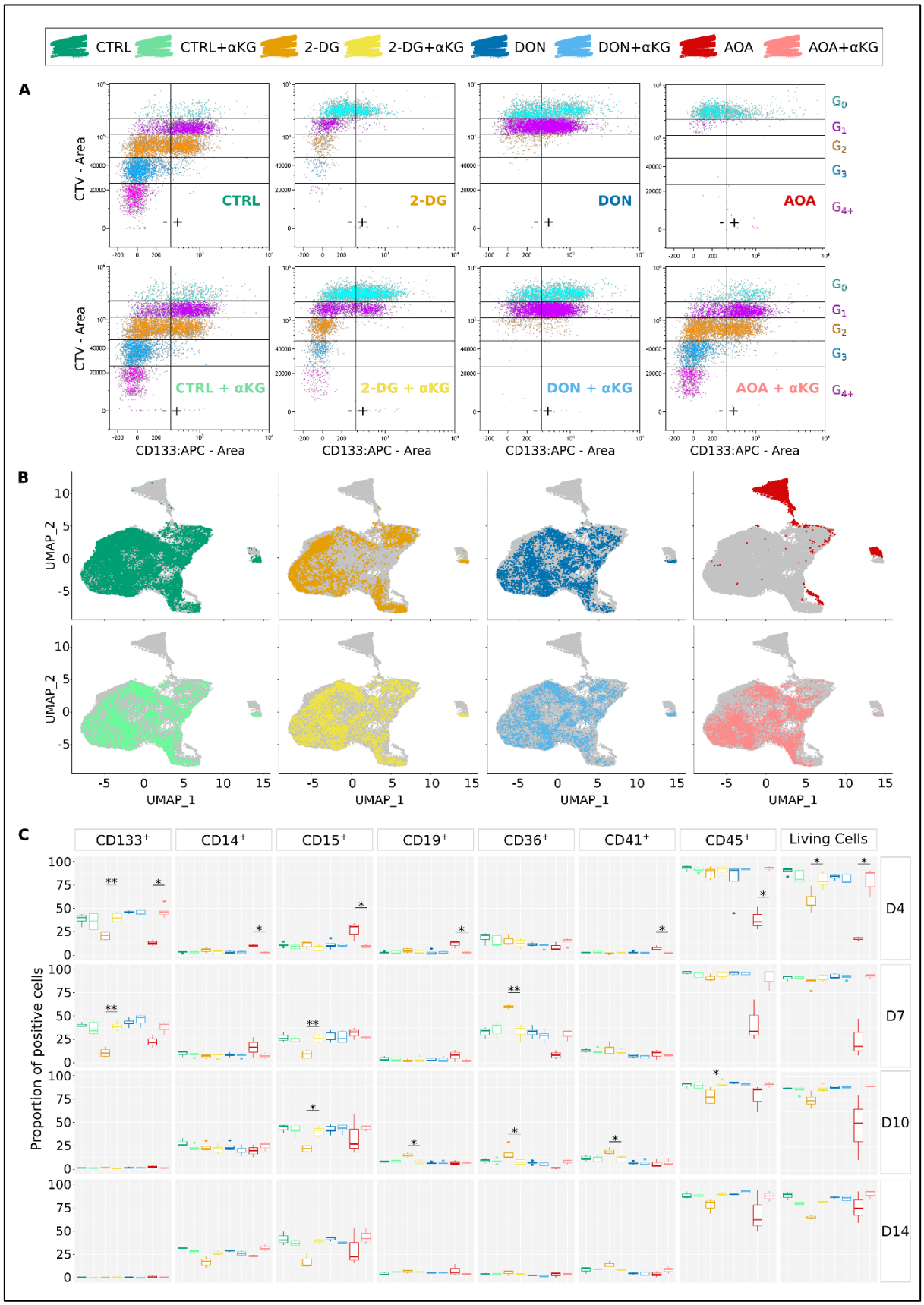
CTRL
CTRL+αKG
2-DG
2-DG+αKG
DON
DON+αKG
AOA
AOA+αKG
A
CTV - Area
CD133:APC - Area
CTRL
2-DG
DON
AOA
CTRL + αKG
2-DG + αKG
DON + αKG
AOA + αKG
G0
G1
G2
G3
G4+
B
UMAP_2
UMAP_1
C
CD133+
CD14+
CD15+
CD19+
CD36+
CD41+
CD45+
Living Cells
Proportion of positive cells
D4
D7
D10
D14

Supporting information

S1 Fig

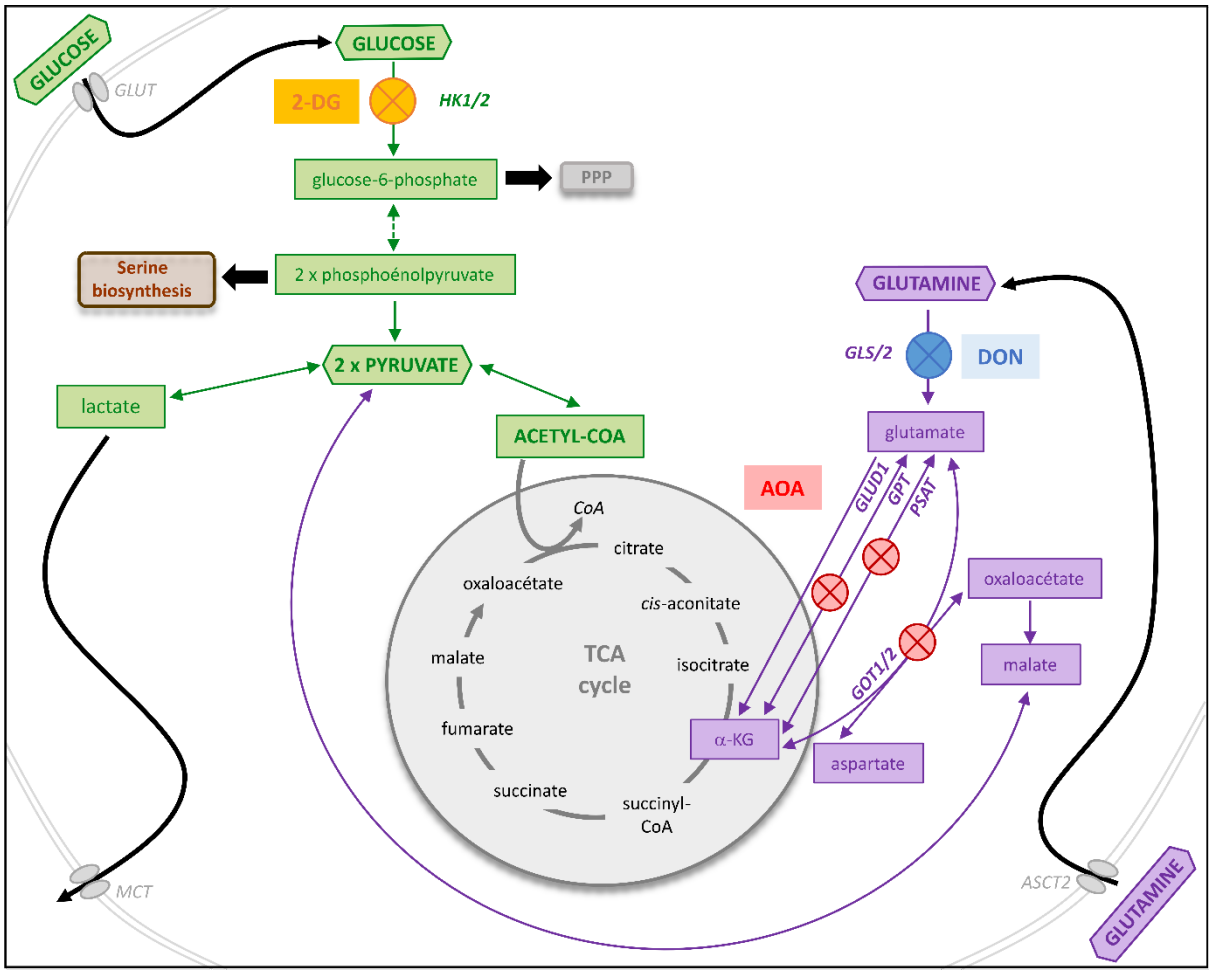

S2 Fig

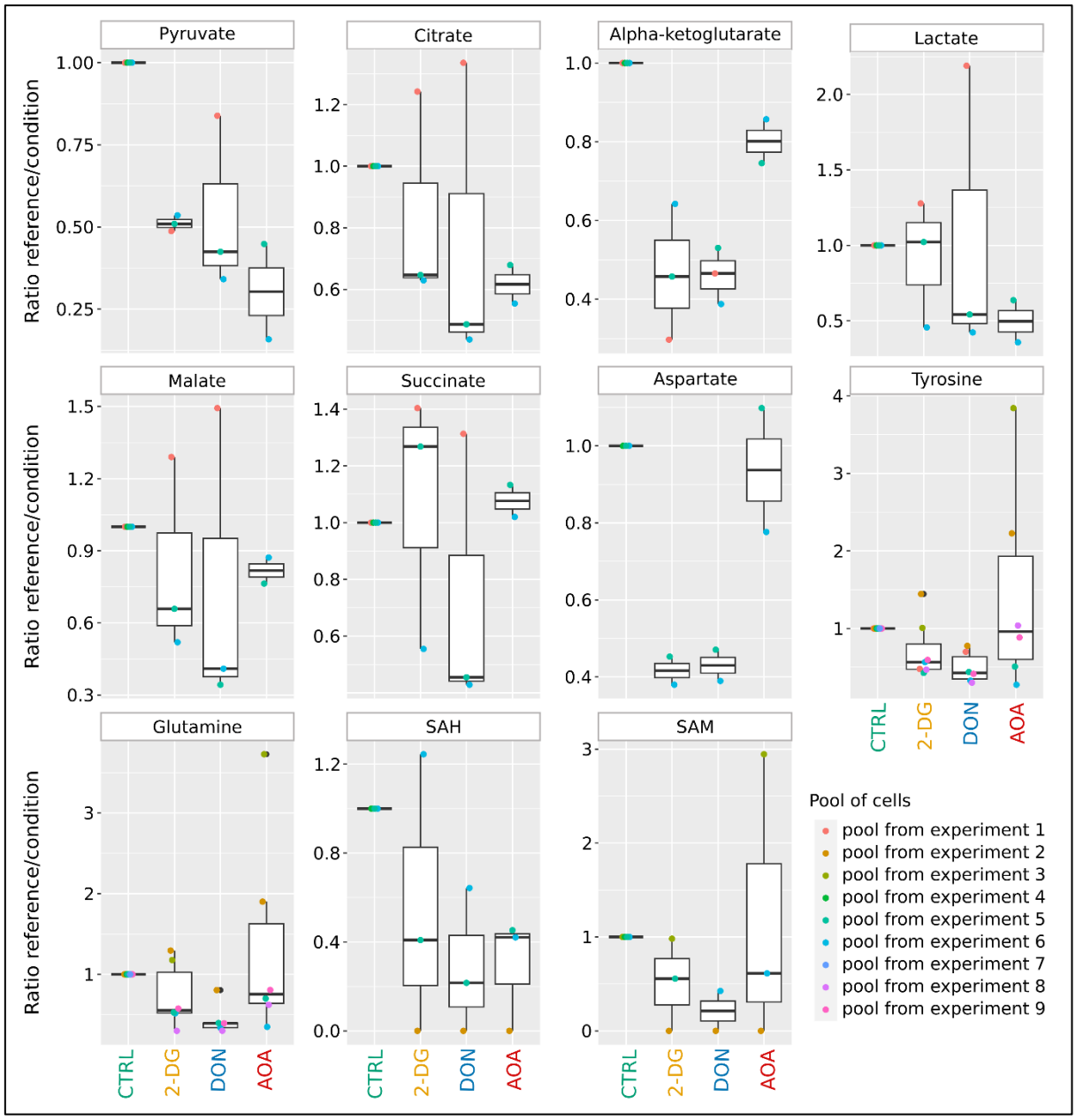
Pyruvate
Citrate
Alpha-ketoglutarate
Lactate
Malate
Succinate
Aspartate
Tyrosine
Glutamine
SAH
SAM
Ratio reference/condition
CTRL
2-DG
DON
AOA
Pool of cells
pool from experiment 1
pool from experiment 2
pool from experiment 3
pool from experiment 4
pool from experiment 5
pool from experiment 6
pool from experiment 7
pool from experiment 8
pool from experiment 9

S3 Fig

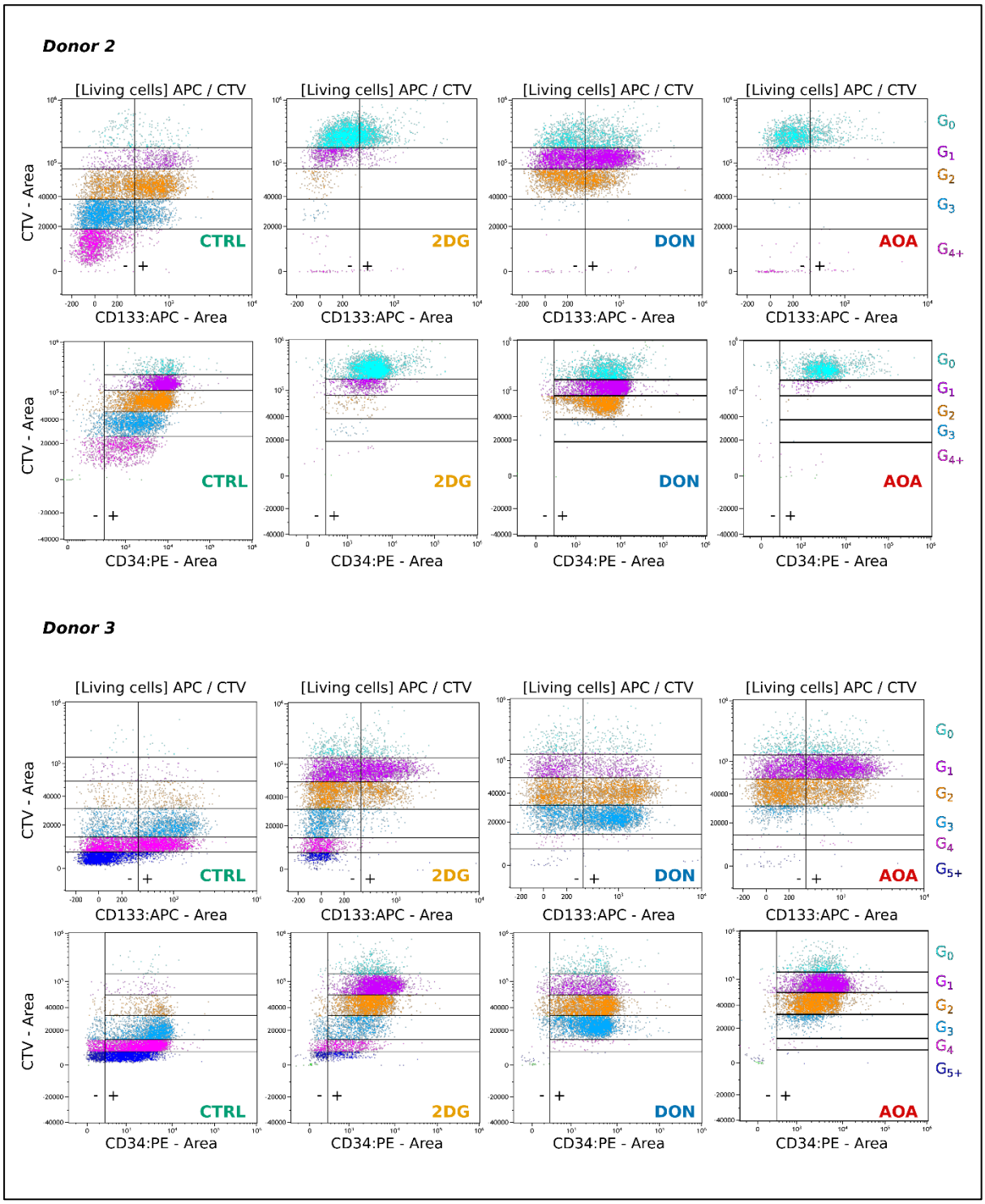
Donor 2
[Living cells] APC / CTV
CTV - Area
CD133:APC - Area
CD34:PE - Area
CTRL
2DG
DON
AOA
G0
G1
G2
G3
G4+
Donor 3
G4
G5+

S4 Fig

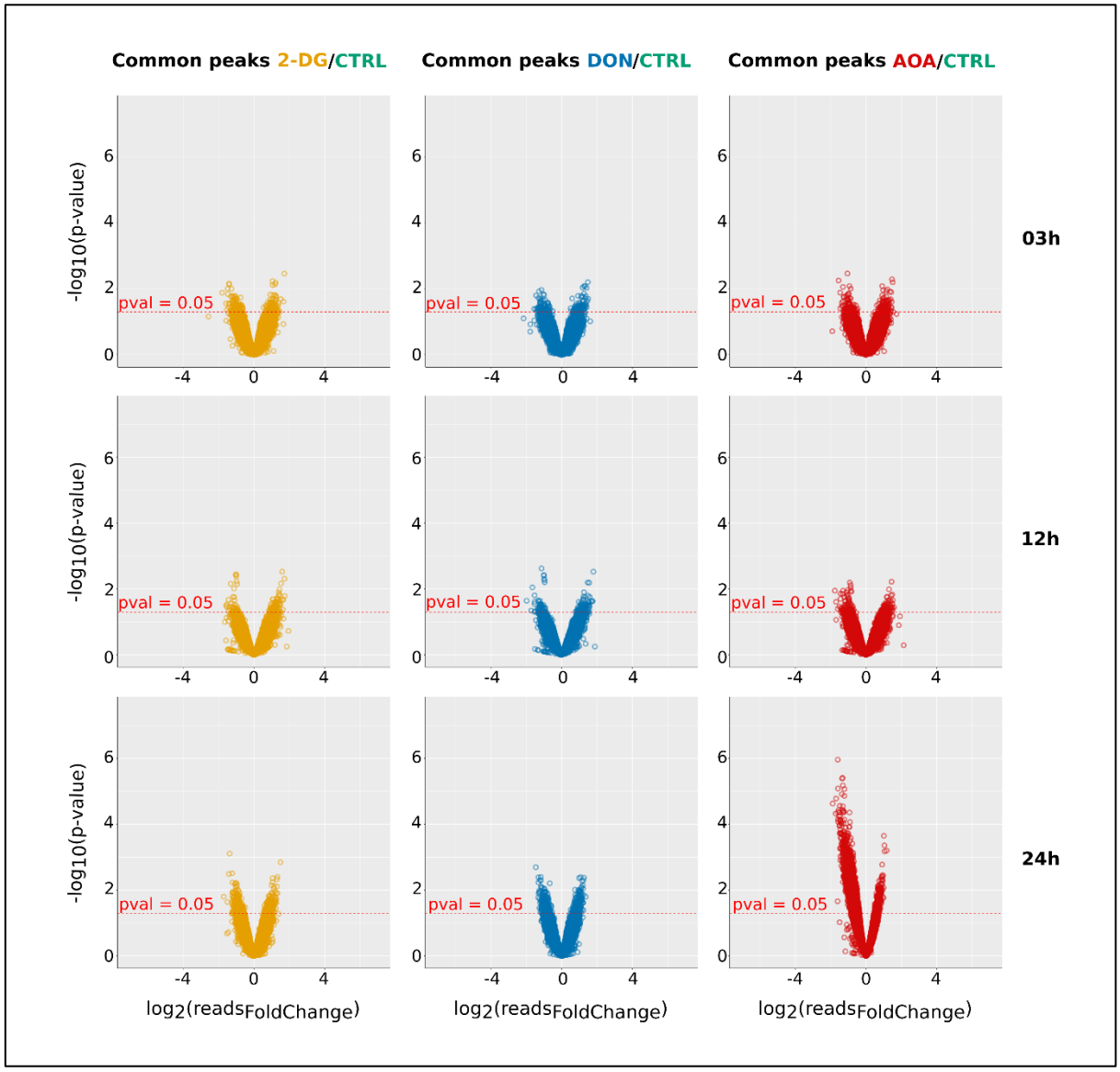
Common peaks 2-DG/CTRL
Common peaks DON/CTRL
Common peaks AOA/CTRL
03h
12h
24h
-log10(p-value)
pval = 0.05
log2(readsFoldChange)

S5 Fig

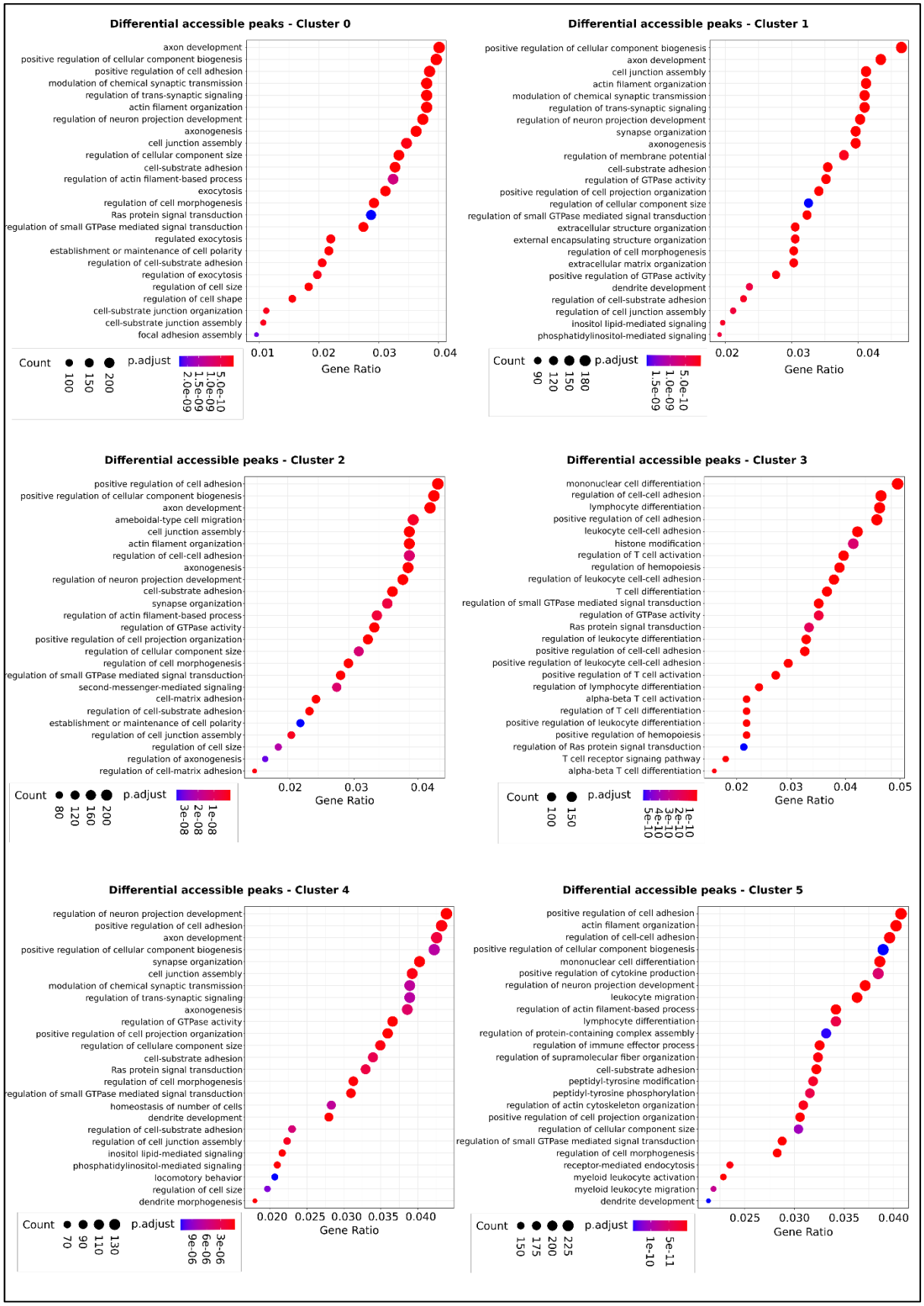
Differential accessible peaks - Cluster 0
axon development
positive regulation of cellular component biogenesis
positive regulation of cell adhesion
modulation of chemical synaptic transmission
regulation of trans-synaptic signaling
actin filament organization
regulation of neuron projection development
axonogenesis
cell junction assembly
regulation of cellular component size
cell-substrate adhesion
regulation of actin filament-based process
exocytosis
regulation of cell morphogenesis
Ras protein signal transduction
regulation of small GTPase mediated signal transduction
regulated exocytosis
establishment or maintenance of cell polarity
regulation of cell-substrate adhesion
regulation of exocytosis
regulation of cell size
regulation of cell shape
cell-substrate junction organization
cell-substrate junction assembly
focal adhesion assembly
0.01 0.02 0.03 0.04
Gene Ratio
Count 100 150 200
p.adjust 5.0e-10 1.0e-09 1.5e-09 2.0e-09
Differential accessible peaks - Cluster 1
positive regulation of cellular component biogenesis
axon development
cell junction assembly
actin filament organization
modulation of chemical synaptic transmission
regulation of trans-synaptic signaling
regulation of neuron projection development
synapse organization
axonogenesis
regulation of membrane potential
cell-substrate adhesion
regulation of GTPase activity
positive regulation of cell projection organization
regulation of cellular component size
regulation of small GTPase mediated signal transduction
extracellular structure organization
external encapsulating structure organization
regulation of cell morphogenesis
extracellular matrix organization
positive regulation of GTPase activity
dendrite development
regulation of cell-substrate adhesion
regulation of cell junction assembly
inositol lipid-mediated signaling
phosphatidylinositol-mediated signaling
0.02 0.03 0.04
Gene Ratio
Count 90 120 150 180
p.adjust 5.0e-10 1.0e-09 1.5e-09
Differential accessible peaks - Cluster 2
positive regulation of cell adhesion
positive regulation of cellular component biogenesis
axon development
ameboidal-type cell migration
cell junction assembly
actin filament organization
regulation of cell-cell adhesion
axonogenesis
regulation of neuron projection development
cell-substrate adhesion
synapse organization
regulation of actin filament-based process
regulation of GTPase activity
positive regulation of cell projection organization
regulation of cellular component size
regulation of cell morphogenesis
regulation of small GTPase mediated signal transduction
second-messenger-mediated signaling
cell-matrix adhesion
regulation of cell-substrate adhesion
establishment or maintenance of cell polarity
regulation of cell junction assembly
regulation of cell size
regulation of axonogenesis
regulation of cell-matrix adhesion
0.02 0.03 0.04
Gene Ratio
Count 80 120 160 200
p.adjust 1e-08 2e-08 3e-08
Differential accessible peaks - Cluster 3
mononuclear cell differentiation
regulation of cell-cell adhesion
lymphocyte differentiation
positive regulation of cell adhesion
leukocyte cell-cell adhesion
histone modification
regulation of T cell activation
regulation of hemopoiesis
regulation of leukocyte cell-cell adhesion
T cell differentiation
regulation of small GTPase mediated signal transduction
regulation of GTPase activity
Ras protein signal transduction
regulation of leukocyte differentiation
positive regulation of cell-cell adhesion
positive regulation of leukocyte cell-cell adhesion
positive regulation of T cell activation
regulation of lymphocyte differentiation
alpha-beta T cell activation
regulation of T cell differentiation
positive regulation of leukocyte differentiation
positive regulation of hemopoiesis
regulation of Ras protein signal transduction
T cell receptor signaing pathway
alpha-beta T cell differentiation
0.02 0.03 0.04 0.05
Gene Ratio
Count 100 150
p.adjust 1e-10 2e-10 3e-10 4e-10 5e-10
Differential accessible peaks - Cluster 4
regulation of neuron projection development
positive regulation of cell adhesion
axon development
positive regulation of cellular component biogenesis
synapse organization
cell junction assembly
modulation of chemical synaptic transmission
regulation of trans-synaptic signaling
axonogenesis
regulation of GTPase activity
positive regulation of cell projection organization
regulation of cellulare component size
cell-substrate adhesion
Ras protein signal transduction
regulation of cell morphogenesis
regulation of small GTPase mediated signal transduction
homeostasis of number of cells
dendrite development
regulation of cell-substrate adhesion
regulation of cell junction assembly
inositol lipid-mediated signaling
phosphatidylinositol-mediated signaling
locomotory behavior
regulation of cell size
dendrite morphogenesis
0.020 0.025 0.030 0.035 0.040
Gene Ratio
Count 70 90 110 130
p.adjust 3e-06 6e-06 9e-06
Differential accessible peaks - Cluster 5
positive regulation of cell adhesion
actin filament organization
regulation of cell-cell adhesion
positive regulation of cellular component biogenesis
mononuclear cell differentiation
positive regulation of cytokine production
regulation of neuron projection development
leukocyte migration
regulation of actin filament-based process
lymphocyte differentiation
regulation of protein-containing complex assembly
regulation of immune effector process
regulation of supramolecular fiber organization
cell-substrate adhesion
peptidyl-tyrosine modification
peptidyl-tyrosine phosphorylation
regulation of actin cytoskeleton organization
positive regulation of cell projection organization
regulation of cellular component size
regulation of small GTPase mediated signal transduction
regulation of cell morphogenesis
receptor-mediated endocytosis
myeloid leukocyte activation
myeloid leukocyte migration
dendrite development
0.025 0.030 0.035 0.040
Gene Ratio
Count 150 175 200 225
p.adjust 5e-11 1e-10

S6 Fig

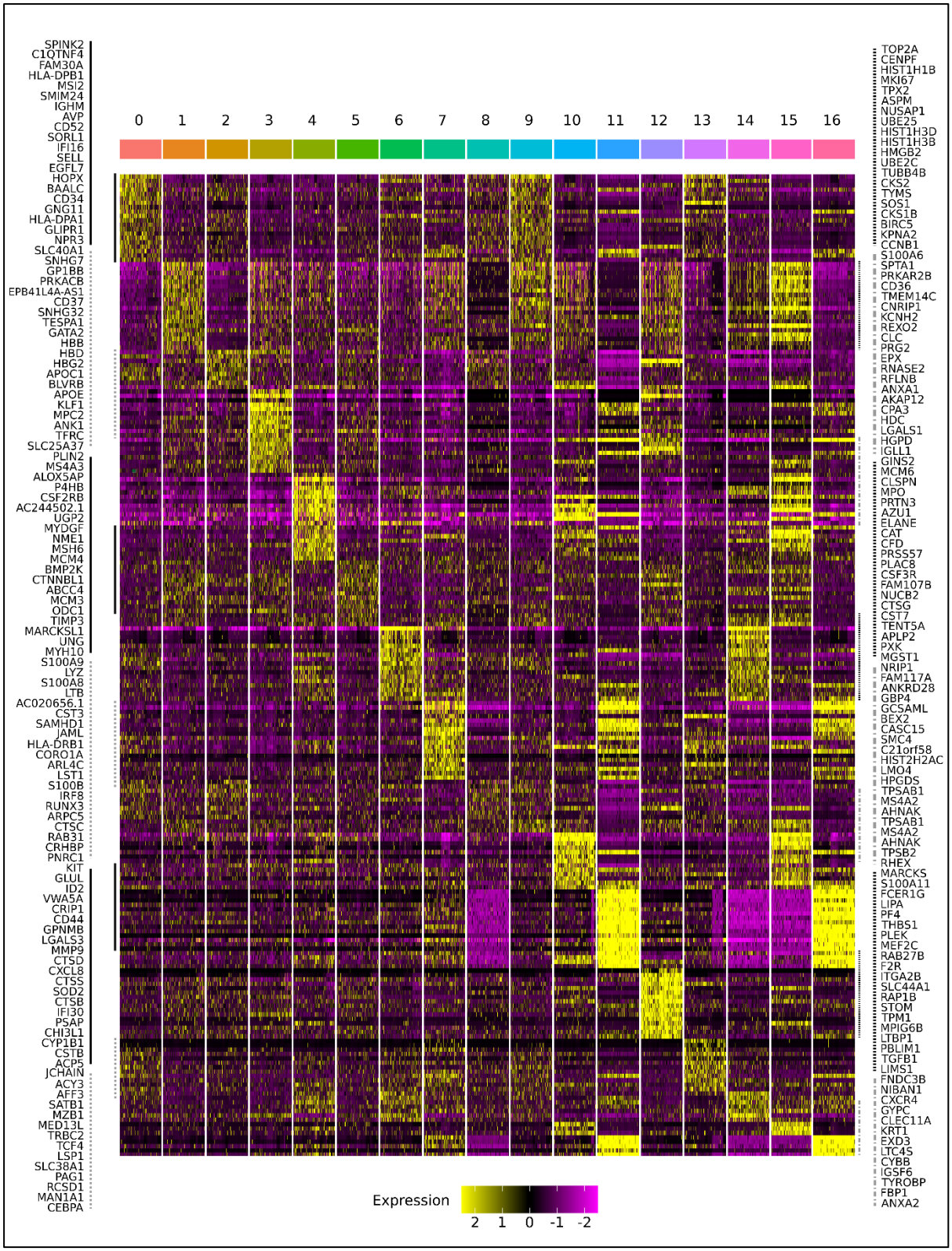
0
1
2
3
4
5
6
7
8
9
10
11
12
13
14
15
16
SPINK2
C1QTNF4
FAM30A
HLA-DPB1
MSI2
SMIM24
IGHM
AVP
CD52
SORL1
IFI16
SELL
EGFL7
HOPX
BAALC
CD34
GNG11
HLA-DPA1
GLIPR1
NPR3
SLC40A1
SNHG7
GP1BB
PRKACB
EPB41L4A-AS1
CD37
SNHG32
TESPA1
GATA2
HBB
HBD
HBG2
APOC1
BLVRB
APOE
KLF1
MPC2
ANK1
TFRC
SLC25A37
PLIN2
MS4A3
ALOX5AP
P4HB
CSF2RB
AC244502.1
UGP2
MYDGF
NME1
MSH6
MCM4
BMP2K
CTNNBL1
ABCC4
MCM3
ODC1
TIMP3
MARCKSL1
UNG
MYH10
S100A9
LYZ
S100A8
LTB
AC020656.1
CST3
SAMHD1
JAML
HLA-DRB1
CORO1A
ARL4C
LST1
S100B
IRF8
RUNX3
ARPC5
CTSC
RAB31
CRHBP
PNRC1
KIT
GLUL
ID2
VWA5A
CRIP1
CD44
GPNMB
LGALS3
MMP9
CTSD
CXCL8
CTSS
SOD2
CTSB
IFI30
PSAP
CHI3L1
CYP1B1
CSTB
ACP5
JCHAIN
ACY3
AFF3
SATB1
MZB1
MED13L
TRBC2
TCF4
LSP1
SLC38A1
PAG1
RCSD1
MAN1A1
CEBPA
TOP2A
CENPF
HIST1H1B
MKI67
TPX2
ASPM
NUSAP1
UBE2S
HIST1H3D
HIST1H3B
HMGB2
UBE2C
TUBB4B
CKS2
TYMS
SOS1
CKS1B
BIRC5
KPNA2
CCNB1
S100A6
SPTA1
PRKAR2B
CD36
TMEM14C
CNRIP1
KCNH2
REXO2
CLC
PRG2
EPX
RNASE2
RFLNB
ANXA1
AKAP12
CPA3
HDC
LGALS1
HGPD
IGLL1
GINS2
MCM6
CLSPN
MPO
PRTN3
AZU1
ELANE
CAT
CFD
PRSS57
PLAC8
CSF3R
FAM107B
NUCB2
CTSG
CST7
TENT5A
APLP2
PXK
MGST1
NRIP1
FAM117A
ANKRD28
GBP4
GCSAML
BEX2
CASC15
SMC4
C21orf58
HIST2H2AC
LMO4
HPGDS
TPSAB1
MS4A2
AHNAK
TPSAB1
MS4A2
AHNAK
TPSB2
RHEX
MARCKS
S100A11
FCER1G
LIPA
PF4
THBS1
PLEK
MEF2C
RAB27B
F2R
TGA2B
SLC44A1
RAP1B
STOM
TPM1
MPIG6B
LTBP1
PBLIM1
TGFB1
LIMS1
FNDC3B
NIBAN1
CXCR4
GYPC
CLEC11A
KRT1
EXD3
LTC4S
CYBB
IGSF6
TYROBP
FBP1
ANXA2
Expression
2
1
0
-1
-2

S7 Fig.

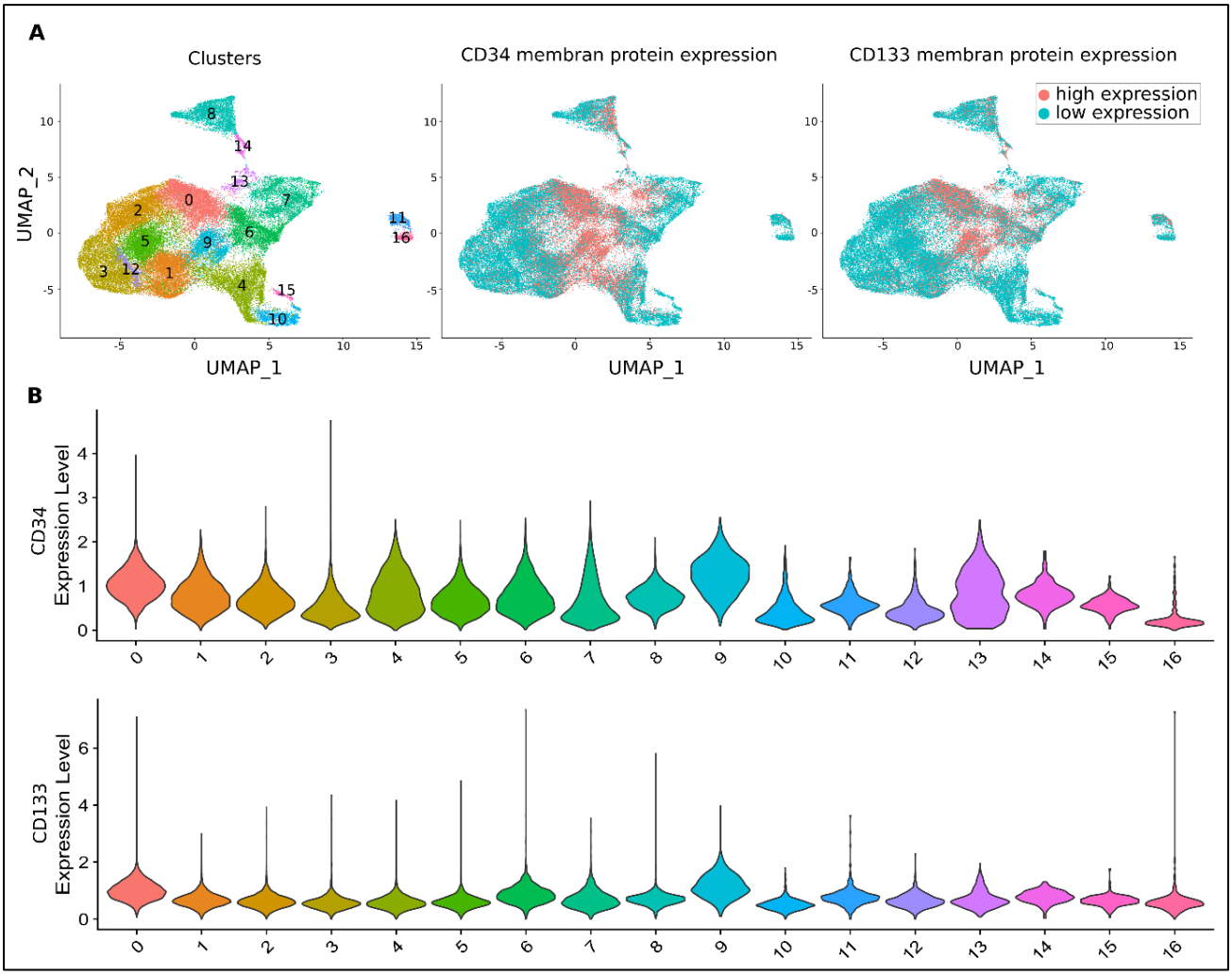
A
Clusters
CD34 membran protein expression
CD133 membran protein expression
high expression
low expression
UMAP_2
UMAP_1
B
CD34 Expression Level
CD133 Expression Level

S8 Fig

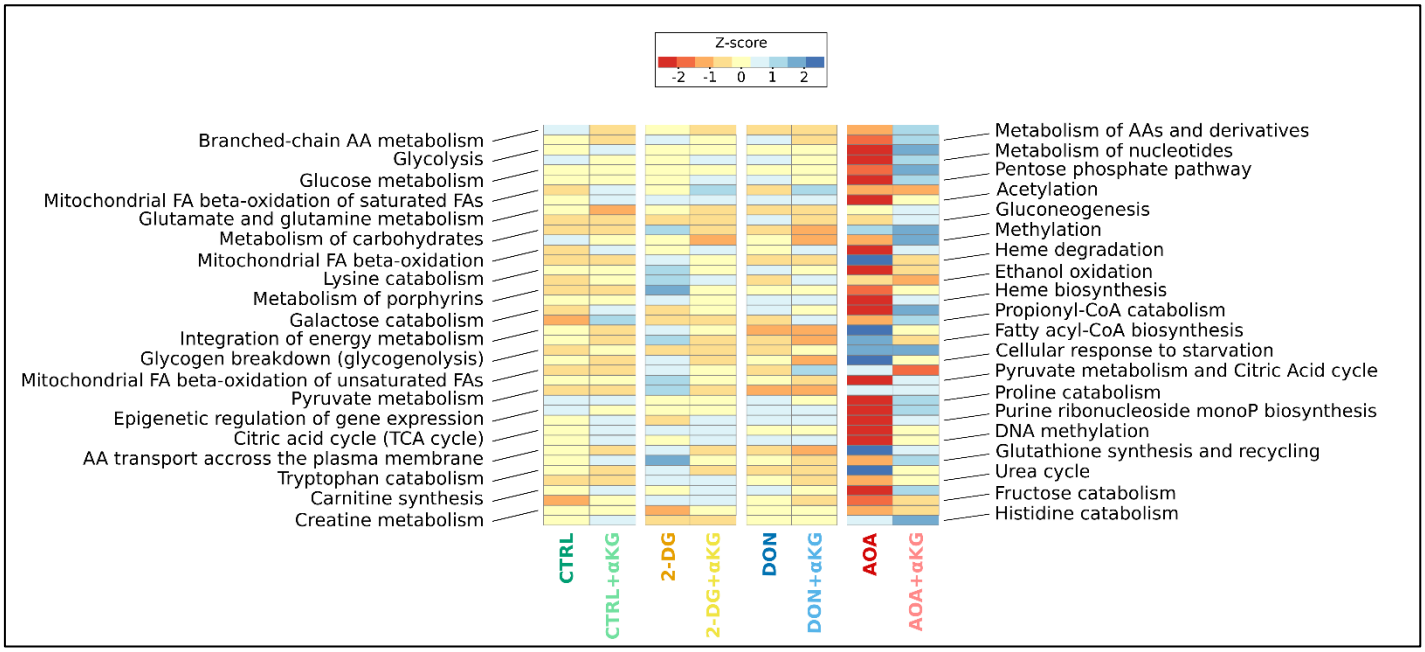
Z-score
-2 -1 0 1 2
Branched-chain AA metabolism
Glycolysis
Glucose metabolism
Mitochondrial FA beta-oxidation of saturated FAs
Glutamate and glutamine metabolism
Metabolism of carbohydrates
Mitochondrial FA beta-oxidation
Lysine catabolism
Metabolism of porphyrins
Galactose catabolism
Integration of energy metabolism
Glycogen breakdown (glycogenolysis)
Mitochondrial FA beta-oxidation of unsaturated FAs
Pyruvate metabolism
Epigenetic regulation of gene expression
Citric acid cycle (TCA cycle)
AA transport accross the plasma membrane
Tryptophan catabolism
Carnitine synthesis
Creatine metabolism
Metabolism of AAs and derivatives
Metabolism of nucleotides
Pentose phosphate pathway
Acetylation
Gluconeogenesis
Methylation
Heme degradation
Ethanol oxidation
Heme biosynthesis
Propionyl-CoA catabolism
Fatty acyl-CoA biosynthesis
Cellular response to starvation
Pyruvate metabolism and Citric Acid cycle
Proline catabolism
Purine ribonucleoside monoP biosynthesis
DNA methylation
Glutathione synthesis and recycling
Urea cycle
Fructose catabolism
Histidine catabolism
CTRL
CTRL+αKG
2-DG
2-DG+αKG
DON
DON+αKG
AOA
AOA+αKG

S9 Fig

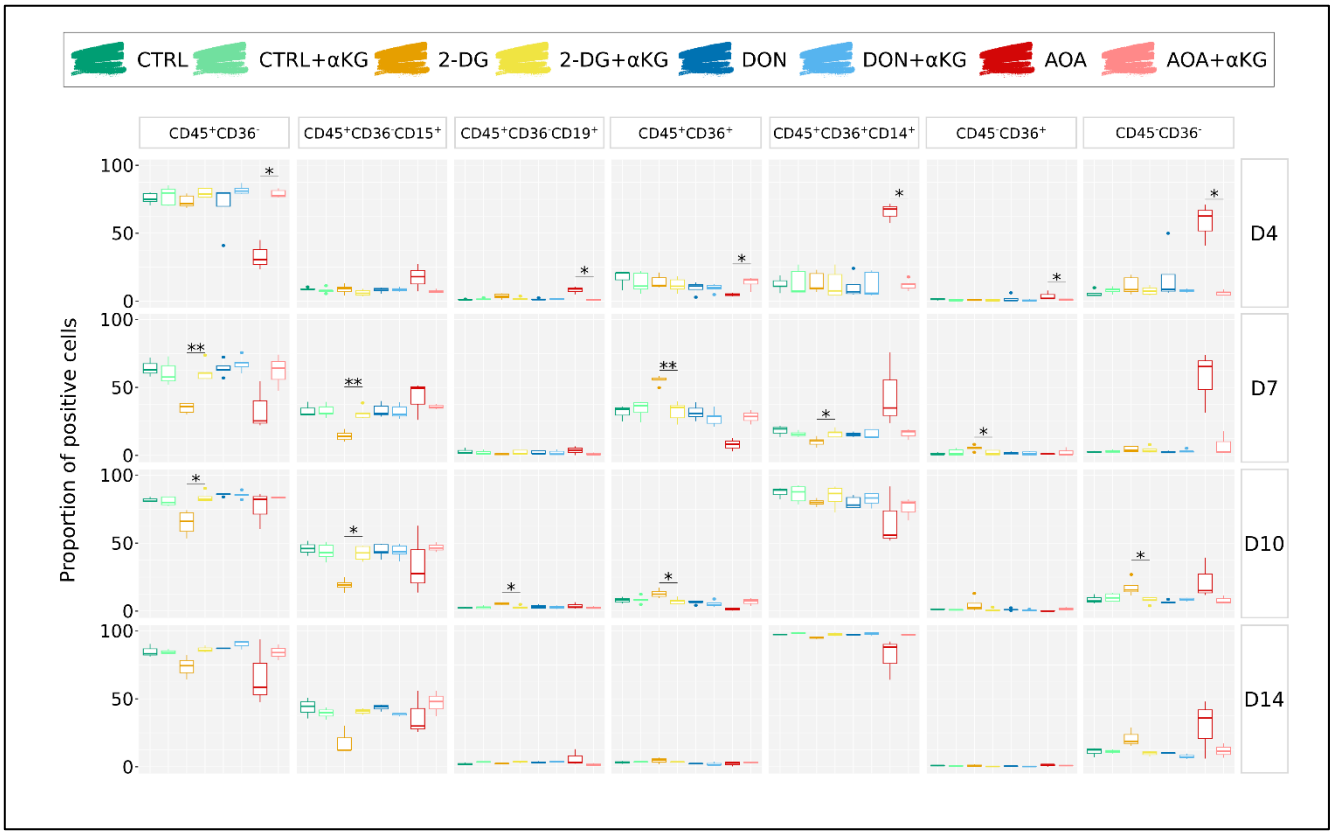
CTRL
CTRL+αKG
2-DG
2-DG+αKG
DON
DON+αKG
AOA
AOA+αKG
CD45⁺CD36⁻
CD45⁺CD36⁻CD15⁺
CD45⁺CD36⁻CD19⁺
CD45⁺CD36⁺
CD45⁺CD36⁺CD14⁺
CD45⁻CD36⁺
CD45⁻CD36⁻
Proportion of positive cells
100
50
0
D4
D7
D10
D14

Figures legends

S1 Fig. Schematic representation of major metabolic pathways and the point of action of the inhibitors. Key steps of glycolysis are highlighted in green, while those of glutaminolysis are marked in violet. Some steps in glycolysis are replaced by a dashed arrow. Colored blocked circles indicate inhibition. 2-DG, an analogue of D-glucose, generates 2-DG-P when phosphorylated by the HK2 enzyme. This molecule is not recognized by subsequent glycolytic enzymes. DON acts as an antagonist of glutamine, irreversibly blocking glutamine-utilizing enzymes, including glutaminases that catalyze glutamine deamination into glutamate during glutaminolysis. AOA is a non-selective inhibitor of transaminases, impeding several pathways converting glutamate into α-ketoglutarate during glutaminolysis.

Fig 1. Experimental strategy and disturbances in cell behavior during early metabolic perturbation.
(A) Experimental strategy: Human cord blood derived $CD34^+$ cells were cultured with or without one of the following metabolic inhibitors: DON 2.5µM, AOA 1.9mM or 2-DG 1mM. Mass spectrometry was performed on cells at 24h to confirm the metabolic perturbation. The chromatin accessibility profile was analyzed by bulk ATAC-seq at 0h, 3h, 12h and 24h and by single-cell ATAC-seq at 24h. Cell's transcriptomes and phenotypes were analyzed by scRNA-seq and cytometry with generations tracking marker at 96h. Continuous observations of the cells were performed during around 160h using time-lapse microscopy. The long-term effects on differentiation were assessed by cytometry at 168h, 240h and 336h after inhibitor removal.
(B) Membrane expression of CD133 and CD34 multipotent markers and CTV labeling across cells generations at 96h. Results obtained from the cells of a representative donor are shown. Generations are indicated by the different colors. G0 is the parental generation. Positive and negative populations are delimited by a vertical line and -/+ signs. Decreased of mean fluorescence intensity (MFI) can be detected by the population shift on the left on the x axis. Other examples are shown on **S2 Fig**. Detailed proportions of positive populations and MFIs per generation are shown on **S2 Table.**
(C) Cumulative number of living- and dead cells and the total number of cell divisions during the first 160 hours based on the time-lapse records. Each experimental condition is represented by a curve. Color codes are available under the graphs.
(D) Switch rates of the cells depending on their culture condition as detected by time-lapse records. This rate is calculated by dividing the number of morphologic switches by the cell cycle duration. The closer it is to 1, the more the cell has changed morphology during its cycle. P-values of pairwise comparisons using Wilcoxon test are indicated. The two successive snapshots on the right panel show the morphological switch of two cells.

S2 Fig. Mass spectrometry measurement of 11 key metabolites in pools of cells cultured in the presence or absence of metabolic inhibitors. Each pool of cells is composed of at least two distinct donors. For each condition, the metabolite measurement encompasses a minimum of two cell pools. To be able to compare different experiments, data were

normalized on the control condition set to 1 as described in **Material and Methods**. Metabolites levels are strongly and differently affected by the inhibitors used. Very few metabolites present similar levels between control and inhibitors. Moreover, cellular responses to the same inhibitor can be close (as observed for pyruvate in the 2-DG condition) but they can also exhibit significant variability (as seen for pyruvate in DON condition) highlighting their remarkable flexibility to respond to environmental changes.

S3 Fig. Flow cytometry measurement of CD133 and CD34 membrane protein combined with generation tracking at 96h for donor2 and donor3.

S1 Table. Summary of the flow cytometry data combined with generation tracking at 96h for all three donors. This table indicates the total number of cells, the number of $CD133^+$ cells and the number of $CD34^+$ cells per generation as well as the proportion the corresponding generation represent and MFI (mean fluorescence intensity). The proliferation index and the total proportion of living cell per condition is also indicated. The usual conditions are presented (CTRL, 2-DG, DON, AOA, CTRL+αKG, 2-DG+αKG, DON+αKG, AOA+αKG).

S1 Movie. Representative examples of time-lapse recording for the four conditions. The videos have been accelerated to 20 frames per second. Due to fogging up of the camera lens, a very brief interruption is noticeable during recording (with a maximum loss of 2 minutes). Notable events as cell death and cell division are highlighted with to kind of arrow on the videos.

Fig 2. Bulk and single-cell ATAC-seq analysis of chromatin accessibility at 24h after the start of metabolic inhibitor's exposure. 00h Xvivo condition corresponds to cells cultured in a medium without early cytokines, before stimulation. (A) Total number of accessible regions (peaks) detected in all three independent donors at four different time points and in four culture conditions as determined by bulk ATAC-seq. Chromatin decompaction occurs in all conditions between 00h and 03h, timing at which the highest number of peaks is reached. AOA-treated cells are the only one to display a noticeable recompaction at 24h. (B) Principal Component Analysis based on differential accessibility analysis of bulk ATAC-seq data. Each point is defined by its color corresponding to its condition and its shape indicating the associated timing. (C) UMAP visualization of the scATAC-seq data at 24h. Each dot represents a cell. Grey profile represents the shape of the total population when all conditions are merged. Color dots represents the cells of the global population corresponding to the studied condition (CTRL, 2-DG, DON or AOA). (D) Clusters identification based on UMAP representation and Louvain algorithm (resolution 0.25). A normalization step was performed before analyzing cell's distribution in clusters to consider the same total number of cells for each condition. All conditions were normalized to 1000 cells. (E) Cell's distribution in scATAC-seq clusters depending on their culture condition.

S4 Fig. Volcano plot representations of bulk ATAC-seq data. The plots displayed the quantitative changes observed in the size of common peaks detected two conditions (CTRL and 2-DG on the left, CTRL and DON in the middle and CTRL and AOA on the right) at each

time point. Each point represents the difference between the size of a peak detected in both conditions (as log2 fold change of the number of reads on the horizontal axis) and the p-value of the change (as log10 of the p-value on the vertical axis). The threshold of p-value = 0.05 is indicated by red spotted line in each plot. Note the significant decrease in peak size compared to control for AOA-treated cells at 24h.

S2 Table. **Statistic summary of the number of peaks per cell detected in scATAC-seq analysis**. This table indicates the minimum, maximum, median and mean number of peaks per cell as well as the total number of studied cells for each condition.

S5 Fig. GO enrichment analysis of the six biggest clusters from scATAC-seq at 24h. Lists of differentially accessible regions for each cluster compared to all the others were extracted and gene ontology analysis was performed on it. A threshold on p-value was set at 0.05 and the 25 top categories were displayed on the dot plots.

Fig 3. Differential gene expression in control and inhibitor treated cells at 96h as determined by scRNA-seq transcriptome analysis. (A) UMAP of the merged scRNA-seq data. Each dot represents a single cell. The same UMAP is reproduced 4 times to highlight the cells of only one of the 4 conditions at the same time. The color code is indicated on the top of the figure. All the other cells are grey. (B) The same UMAP map as in (A) is represented to allow the identification of individual clusters. The cluster were numbered from the largest to the smallest. The numbers, the color codes and the relative size of the clusters are indicated in the inset on the right. (E) Histogram of the cluster compositions. The color codes for the control and inhibitor treated conditions are identical as in (A). Note, that while the cell populations treated with DON and 2-DG overlap with the control population, AOA-treated cells appear to have developed entirely distinct expression profiles. (D) ReactomeGSA's pathway analysis of 40 pathways of interest. The pathway names are given on the two sides of the heat-map and the color code for the Z-score of the expression levels is on the right inset. Note the very different pathway profile of the AOA-treated cells.

S6 Fig. **Heat map representation of the highly expressed genes specific for each cluster**. The number of the clusters and their corresponding color code are indicated on the top and the gene names are on the two sides. The continuous or dotted vertical lines indicate gene groups highlighted by the same type of line on the same sides of the heat-map. The expression level color code is displayed on the bottom of the figure. Note that each cluster appears highly distinct from the others, characterized by specific sets of genes that are either underexpressed or overexpressed.

S7 Fig. CD133 and CD34 membrane protein levels on the cells used for scRNA sequencing using CITE-seq analysis. (A) UMAP visualization of the global cell population, all conditions combined. The left panel shows the cluster numbers. The middle and the right panels show the level of the CD34 and CD133 proteins respectively. The color code for "high" and "low" expression is indicated in the inset on the right. (B) Violin plots of CD34 and CD133 protein expression levels in each cluster.

S3 Table. GO analysis of differentially expressed genes in the pairwise comparisons between control and inhibitor treated cells. The first column of the table gives an indication on the list of markers used for the GO analysis. For example, "CTRL>2DG" indicates that the markers used are the ones enriched in the CTRL condition compared to 2-DG. Two methods were used to extract specific markers for each condition and indicated in the "Method" column: the manual average outliers' identification method ("ego_avg_gene") and the FindMarkers function from Seurat package ("ego_FindMarkers_gene") as explained in **Material and Methods**. Terms related to hematopoietic lineage and associated functions are highlighted in red to enhance the table's readability.

Fig 4. Analysis of the cell differentiation potential in long-term *in vitro* cultures at day 4, 7, 10 and 14 – simple markers. Results of several experiments are summarized as boxplots, displaying the proportion of positive cells for each individual marker. Wilcoxon statistical test was performed on pairwise comparisons (control vs inhibitor). (A) Proportion of living cells for each condition over time. AOA-treated cells displayed a high heterogeneity of sensibility in response to the inhibitor compared to the other conditions. (B) Proportion of cells displaying the individual markers on their membrane. CD133 is considered as a multipotent marker. CD14 and CD15 are associated to myeloid cells, respectively monocytes/macrophages and granulocytes/monocytes. CD19 is a marker commonly found on B lymphocytes and CD36 mostly on erythrocytes progenitors. CD41 is characteristic of platelets and CD45 is present on the surface of all nucleated hematopoietic cells.

Fig 5. Analysis of the cell differentiation potential in long-term *in vitro* cultures at day 4, 7, 10 and 14 – combined markers. Results of several experiments are summarized as boxplots displaying the proportion of positive cells for each combination of markers: $CD45^{+}CD36^{-}$ for granulocytes and lymphocytes $CD45^{+}CD36^{-}CD15^{+}$ for granulocytic cells, $CD45^{+}CD36^{-}CD19^{+}$ for B lymphocytes, $CD45^{+}CD36^{+}$ for monocytes and macrophages, $CD45^{+}CD36^{+}CD14^{+}$ for monocytes, CD45-CD36+ corresponding mostly to erythrocytes progenitors and $CD45^{-}CD36^{-}$ to mature erythrocytes. Wilcoxon statistical test was performed on pairwise comparisons (control vs inhibitor).

Fig 6. Rescue experiments with αKG. (A) CD133 expression and generations tracking measured by flow cytometry at 96hrs. Generations are indicated by the different colors. Positive and negative populations are delimited by a vertical line and -/+ signs. Detailed proportions of positive populations and MFI per generation for CD133 but also CD34 marker are available on **S2 Table.** In addition to restoring viability, the addition of αKG in the culture medium seems to completely counteract the inhibition induced by AOA. (B) UMAP of the scRNA-seq data with or without αKG. Each dot represents a cell. Grey profile represents the shape of the total population when all conditions are merged. Cells treated with different inhibitors are highlighted by their corresponding colors. Individual clusters are not highlighted, please refer to Fig.3B. The addition of αKG restored gene expression profile of 2-DG-treated cells, but only partially in AOA-treated cells. (C) Proportion of positive cells for individual markers from long-term cytometry experiment at day 4, 7, 10 and 14. Wilcoxon

statistical test was performed on pairwise comparisons between condition and condition + αKG. All markers seem to be expressed at the same level as in control when αKG is added with the inhibitors.

S8 Fig. Comparison of 40 pathways levels between control cells, inhibitors treated cells and rescued cells. The analysis was made using ReactomeGSA database.

S9 Fig. Analysis of marker combinations in the long-term differentiation experiments using cytometry at day 4, 7, 10 and 14 in control, inhibitor treated and αKG rescued cells. Wilcoxon statistical test was performed on pairwise comparisons between condition and condition + α-ketoglutarate.

S4 Table. GO analysis on differentially expressed genes in the pairwise comparisons between condition and condition plus α-ketoglutarate. The first column of the table gives an indication on the list of markers used for the GO analysis. For example, "2DG>2DGaKG" indicates that the markers used are the ones enriched in the 2-DG condition compared to 2-DG+αKG. Two methods were used to extract specific markers for each condition and indicated in the "Method" column: the manual average outliers' identification method ("ego_avg_gene") and the FindMarkers function from Seurat package ("ego_FindMarkers_gene") as explained in **Material and Methods**. Terms related to hematopoietic lineage and associated functions are highlighted in red to enhance the table's readability.

References

1. Parmentier R, Racine L, Moussy A, Chantalat S, Sudharshan R, Papili Gao N, et al. Global genome decompaction leads to stochastic activation of gene expression as a first step toward fate commitment in human hematopoietic cells. Huang S, editor. PLOS Biol. 2022;20: e3001849. doi:10.1371/journal.pbio.3001849

2. Martínez-Reyes I, Chandel NS. Mitochondrial TCA cycle metabolites control physiology and disease. Nat Commun. 2020;11: 102. doi:10.1038/s41467-019-13668-3

3. Ye C, Tu BP. Sink into the Epigenome: Histones as repositories that influence cellular metabolism. Trends Endocrinol Metab TEM. 2018;29: 626–637. doi:10.1016/j.tem.2018.06.002

4. Katan-Khaykovich Y, Struhl K. Dynamics of global histone acetylation and deacetylation in vivo: rapid restoration of normal histone acetylation status upon removal of activators and repressors. Genes Dev. 2002;16: 743–752. doi:10.1101/gad.967302

5. Yamagata Y, Szabó P, Szüts D, Bacquet C, Arányi T, Paldi A. Rapid turnover of DNA methylation in human cells. Epigenetics. 2012;7: 141–145. doi:10.4161/epi.7.2.18906

6. Schofield Z, Meloni G, Tran P, Zerfass Christian, Sena G, Hayashi Y, et al. Bioelectrical understanding and engineering of cell biology. J R Soc Interface. 2020 [cited 29 Aug 2023]. Available: https://royalsocietypublishing.org/doi/10.1098/rsif.2020.0013

7. Li X, Hui S, Mirek ET, Jonsson WO, Anthony TG, Lee WD, et al. Circulating metabolite homeostasis achieved through mass action. Nat Metab. 2022;4: 141–152. doi:10.1038/s42255-021-00517-1

8. Walsh CT, Tu BP, Tang Y. Eight Kinetically Stable but Thermodynamically Activated Molecules that Power Cell Metabolism. Chem Rev. 2018;118: 1460–1494. doi:10.1021/acs.chemrev.7b00510

9. Moussy A, Cosette J, Parmentier R, Silva C da, Corre G, Richard A, et al. Integrated time-lapse and single-cell transcription studies highlight the variable and dynamic nature of human hematopoietic cell fate commitment. PLOS Biol. 2017;15: e2001867. doi:10.1371/journal.pbio.2001867

10. Romero-Moya D, Bueno C, Montes R, Navarro-Montero O, Iborra FJ, López LC, et al. Cord blood-derived CD34+ hematopoietic cells with low mitochondrial mass are enriched in hematopoietic repopulating stem cell function. Haematologica. 2013;98: 1022–1029. doi:10.3324/haematol.2012.079244

11. Zhang CC, Sadek HA. Hypoxia and Metabolic Properties of Hematopoietic Stem Cells. Antioxid Redox Signal. 2014;20: 1891–1901. doi:10.1089/ars.2012.5019

12. Ito K, Suda T. Metabolic requirements for the maintenance of self-renewing stem cells. Nat Rev Mol Cell Biol. 2014;15: 243–256. doi:10.1038/nrm3772

13. Arranz L, Urbano-Ispizúa A, Méndez-Ferrer S. Mitochondria underlie different metabolism of hematopoietic stem and progenitor cells. Haematologica. 2013;98: 993–995. doi:10.3324/haematol.2013.084293

14. Suda T, Takubo K, Semenza GL. Metabolic regulation of hematopoietic stem cells in the hypoxic niche. Cell Stem Cell. 2011;9: 298–310. doi:10.1016/j.stem.2011.09.010

15. Richard A, Vallin E, Romestaing C, Roussel D, Gandrillon O, Gonin-Giraud S. Erythroid differentiation displays a peak of energy consumption concomitant with glycolytic metabolism rearrangements. PLOS ONE. 2019;14: e0221472. doi:10.1371/journal.pone.0221472

16. Oburoglu L, Romano M, Taylor N, Kinet S. Metabolic regulation of hematopoietic stem cell commitment and erythroid differentiation. Curr Opin Hematol. 2016;23: 198–205. doi:10.1097/MOH.0000000000000234

17. Groelke J, Amos H. Transaminase inhibitors block glycolysis and G1 to S phase progression in chick embryo fibroblasts: Reversal by α-keto acids. J Cell Physiol. 1984;119: 133–136. doi:10.1002/jcp.1041190121

18. Oburoglu L, Mansell E, Woods N-B. Glutamine metabolism regulates endothelial to hematopoietic transition and hematopoietic lineage specification. Sci Rep. 2021;11: 17589. doi:10.1038/s41598-021-97194-7

19. Walvekar A, Rashida Z, Maddali H, Laxman S. A versatile LC-MS/MS approach for comprehensive, quantitative analysis of central metabolic pathways. Wellcome Open Res. 2018;3: 122. doi:10.12688/wellcomeopenres.14832.1

20. Griss J, Viteri G, Sidiropoulos K, Nguyen V, Fabregat A, Hermjakob H. ReactomeGSA - Efficient Multi-Omics Comparative Pathway Analysis. Mol Cell Proteomics. 2020;19: 2115–2125. doi:10.1074/mcp.TIR120.002155

21. Mistry JJ, Hellmich C, Moore JA, Jibril A, Macaulay I, Moreno-Gonzalez M, et al. Free fatty-acid transport via CD36 drives β-oxidation-mediated hematopoietic stem cell response to infection. Nat Commun. 2021;12: 7130. doi:10.1038/s41467-021-27460-9

22. Ye H, Adane B, Khan N, Sullivan T, Minhajuddin M, Gasparetto M, et al. Leukemic Stem Cells Evade Chemotherapy by Metabolic Adaptation to an Adipose Tissue Niche. Cell Stem Cell. 2016;19: 23–37. doi:10.1016/j.stem.2016.06.001

23. Qi L, Martin-Sandoval M, Merchant S, Zhao Z, Agathocleous M, Morrison S. Aspartate availability limits hematopoietic stem cell function during hematopoietic regeneration. Cell Stem Cell. 2021 [cited 11 Sep 2023]. doi:https://doi.org/10.1016/j.stem.2021.07.011

24. Tsukada Y, Fang J, Erdjument-Bromage H, Warren ME, Borchers CH, Tempst P, et al. Histone demethylation by a family of JmjC domain-containing proteins. Nature. 2006;439: 811–816. doi:10.1038/nature04433

25. Wu X, Zhang Y. TET-mediated active DNA demethylation: mechanism, function and beyond. Nat Rev Genet. 2017;18: 517–534. doi:10.1038/nrg.2017.33

26. TeSlaa T, Chaikovsky AC, Lipchina I, Escobar SL, Hochedlinger K, Huang J, et al. α-Ketoglutarate Accelerates the Initial Differentiation of Primed Human Pluripotent Stem Cells. Cell Metab. 2016;24: 485–493. doi:10.1016/j.cmet.2016.07.002

27. Tohyama S, Fujita J, Hishiki T, Matsuura T, Hattori F, Ohno R, et al. Glutamine Oxidation Is Indispensable for Survival of Human Pluripotent Stem Cells. Cell Metab. 2016;23: 663–674. doi:10.1016/j.cmet.2016.03.001

28. Lu V, Teitell MA. Alpha-ketoglutarate: a “magic” metabolite in early germ cell development. EMBO J. 2019 [cited 17 Aug 2023]. Available: https://www.embopress.org/doi/full/10.15252/embj.2018100615

29. Hwang I-Y, Kwak S, Lee S, Kim H, Lee SE, Kim J-H, et al. Psat1-Dependent Fluctuations in α-Ketoglutarate Affect the Timing of ESC Differentiation. Cell Metab. 2016;24: 494–501. doi:10.1016/j.cmet.2016.06.014

30. Nakamura-Ishizu A, Ito K, Suda T. Hematopoietic Stem Cell Metabolism during Development and Aging. Dev Cell. 2020;54: 239–255. doi:10.1016/j.devcel.2020.06.029

31. Tsuchiya M, Brazhnik P, Bizzarri M, Giuliani A. Synchronization between Attractors: Genomic Mechanism of Cell-Fate Change. Int J Mol Sci. 2023;24: 11603. doi:10.3390/ijms241411603

32. Huang S. Cell Lineage Determination in State Space: A Systems View Brings Flexibility to Dogmatic Canonical Rules. PLOS Biol. 2010;8: e1000380. doi:10.1371/journal.pbio.1000380

33. Huang S, Guo Y-P, May G, Enver T. Bifurcation dynamics in lineage-commitment in bipotent progenitor cells. Dev Biol. 2007;305: 695–713. doi:10.1016/j.ydbio.2007.02.036

34. Huang S. Systems biology of stem cells: three useful perspectives to help overcome the paradigm of linear pathways. Philos Trans R Soc B Biol Sci. 2011;366: 2247–2259. doi:10.1098/rstb.2011.0008

35. Baksh SC, Finley LWS. Metabolic Coordination of Cell Fate by α-Ketoglutarate-Dependent Dioxygenases. Trends Cell Biol. 2021;31: 24–36. doi:10.1016/j.tcb.2020.09.010

36. Hu M, Krause D, Greaves M, Sharkis S, Dexter M, Heyworth C, et al. Multilineage gene expression precedes commitment in the hemopoietic system. Genes Dev. 1997;11: 774–785. doi:10.1101/gad.11.6.774

37. Pina C, Fugazza C, Tipping AJ, Brown J, Soneji S, Teles J, et al. Inferring rules of lineage commitment in haematopoiesis. Nat Cell Biol. 2012;14: 287–294. doi:10.1038/ncb2442

38. Nimmo RA, May GE, Enver T. Primed and ready: understanding lineage commitment through single cell analysis. Trends Cell Biol. 2015;25: 459–467. doi:10.1016/j.tcb.2015.04.004

39. Gao NP, Gandrillon O, Páldi A, Herbach U, Gunawan R. Single-cell transcriptional uncertainty landscape of cell differentiation. F1000Research; 2023 Jul. Report No.: 12:426. doi:10.12688/f1000research.131861.2

40. Hamant O, Bhat R, Nanjundiah V, Newman SA. Does resource availability help determine the evolutionary route to multicellularity? Evol Dev. 2019;21: 115–119. doi:10.1111/ede.12287

41. Varahan S, Sinha V, Walvekar A, Krishna S, Laxman S. Resource plasticity-driven carbon-nitrogen budgeting enables specialization and division of labor in a clonal community. eLife. 2020 [cited 17 Aug 2023]. Available: https://elifesciences.org/articles/57609

42. Capp J-P, Thomas F. A Similar Speciation Process Relying on Cellular Stochasticity in Microbial and Cancer Cell Populations. iScience. 2020;23: 101531. doi:10.1016/j.isci.2020.101531

43. Varahan S, Walvekar A, Sinha V, Krishna S, Laxman S. Metabolic constraints drive self-organization of specialized cell groups. Verstrepen KJ, Barkai N, Ackermann M, editors. eLife. 2019;8: e46735. doi:10.7554/eLife.46735

44. Kupiec JJ. A chance-selection model for cell differentiation. Cell Death Differ. 1996;3: 385–390.

45. Kupiec JJ. A Darwinian theory for the origin of cellular differentiation. Mol Gen Genet MGG. 1997;255: 201–208. doi:10.1007/s004380050490

46. Kupiec J-J. The Origin Of Individuals. 2009. Available: https://doi.org/10.1142/6359

47. Paldi A. Stochastic or Deterministic? That is the Question. Org J Biol Sci. 2020;4: 77–79. doi:10.13133/2532-5876/16963

48. Noble D. Cellular Darwinism: Regulatory networks, stochasticity, and selection in cancer development. Prog Biophys Mol Biol. 2021;165: 66–71. doi:10.1016/j.pbiomolbio.2021.06.007

49. Braun E. The unforeseen challenge: from genotype-to-phenotype in cell populations. Rep Prog Phys. 2015;78: 036602. doi:10.1088/0034-4885/78/3/036602

50. Shomar A, Barak O, Brenner N. Cancer progression as a learning process. iScience. 2022;25. doi:10.1016/j.isci.2022.103924

51. Paldi A. Stochastic gene expression during cell differentiation: order from disorder? Cell Mol Life Sci CMLS. 2003;60: 1775–1778. doi:10.1007/s00018-003-23147-z

52. Páldi A. 3 - Random walk across the epigenetic landscape. In: Levine H, Jolly MK, Kulkarni P, Nanjundiah V, editors. Phenotypic Switching. Academic Press; 2020. pp. 53–76. doi:10.1016/B978-0-12-817996-3.00008-6

53. Kim C, Ding X, Allmeroth K, Denzel M, Eming S, Wickström S. Glutamine Metabolism Controls Stem Cell Fate Reversibility and Long-Term Maintenance in the Hair Follicle. Cell Metab. 2020 [cited 17 Aug 2023]. Available: https://www.cell.com/cell-metabolism/fulltext/S1550-4131(20)30424-1

54. Marsboom G, Zhang G-F, Pohl-Avila N, Zhang Y, Yuan Y, Kang H, et al. Glutamine Metabolism Regulates the Pluripotency Transcription Factor OCT4. Cell Rep. 2016;16: 323–332. doi:10.1016/j.celrep.2016.05.089

55. Folmes CDL, Nelson TJ, Martinez-Fernandez A, Arrell DK, Lindor JZ, Dzeja PP, et al. Somatic oxidative bioenergetics transitions into pluripotency-dependent glycolysis to facilitate nuclear reprogramming. Cell Metab. 2011;14: 264–271. doi:10.1016/j.cmet.2011.06.011

56. Niklas KJ. The evolutionary-developmental origins of multicellularity. Am J Bot. 2014;101: 6–25. doi:10.3732/ajb.1300314

57. Niklas KJ, Newman SA. The many roads to and from multicellularity. J Exp Bot. 2020;71: 3247–3253. doi:10.1093/jxb/erz547

58. Furusawa C, Kaneko K. A Dynamical-Systems View of Stem Cell Biology. Science. 2012;338: 215–217. doi:10.1126/science.1224311

59. Cosette J, Moussy A, Paldi A, Stockholm D. Combination of imaging flow cytometry and time-lapse microscopy for the study of label-free morphology dynamics of hematopoietic cells. Cytom Part J Int Soc Anal Cytol. 2017;91: 254–260. doi:10.1002/cyto.a.23064

60. Cosette J, Moussy A, Onodi F, Auffret-Cariou A, Neildez-Nguyen TMA, Paldi A, et al. Single Cell Dynamics Causes Pareto-Like Effect in Stimulated T Cell Populations. Sci Rep. 2015;5: 17756. doi:10.1038/srep17756

61. Stringer C, Wang T, Michaelos M, Pachitariu M. Cellpose: a generalist algorithm for cellular segmentation. Nat Methods. 2021;18: 100–106. doi:10.1038/s41592-020-01018-x

62. Roederer M. Interpretation of cellular proliferation data: Avoid the panglossian. Cytometry A. 2011;79A: 95–101. doi:10.1002/cyto.a.21010

63. Waltman L, van Eck NJ. A smart local moving algorithm for large-scale modularity-based community detection. Eur Phys J B. 2013;86: 471. doi:10.1140/epjb/e2013-40829-0